

## Sand-Mud Tidal Flat Morphodynamics Influenced by Alongshore Tidal Currents

Wang, Yunwei; Wang, Yaping; Yu, Qian; Du, Zhiyun; Wang, Zhengbing ; Gao, Shu

**DOI**

[10.1029/2018JC014550](https://doi.org/10.1029/2018JC014550)

**Publication date**

2019

**Document Version**

Accepted author manuscript

**Published in**

Journal Of Geophysical Research-Oceans

**Citation (APA)**

Wang, Y., Wang, Y., Yu, Q., Du, Z., Wang, Z., & Gao, S. (2019). Sand-Mud Tidal Flat Morphodynamics Influenced by Alongshore Tidal Currents. *Journal Of Geophysical Research-Oceans*, 124(6), 3818-3836. <https://doi.org/10.1029/2018JC014550>

**Important note**

To cite this publication, please use the final published version (if applicable). Please check the document version above.

**Copyright**

Other than for strictly personal use, it is not permitted to download, forward or distribute the text or part of it, without the consent of the author(s) and/or copyright holder(s), unless the work is under an open content license such as Creative Commons.

**Takedown policy**

Please contact us and provide details if you believe this document breaches copyrights. We will remove access to the work immediately and investigate your claim.

# 1 Sand-Mud Tidal Flat Morphodynamics

## 2 Influenced by Alongshore Tidal Currents

3 Yunwei Wang<sup>1</sup>, Ya Ping Wang<sup>2</sup>, Qian Yu<sup>3\*</sup>, Zhiyun Du<sup>3</sup>, Zheng Bing Wang<sup>4,5</sup>, Shu Gao<sup>2</sup>

4 <sup>1</sup> Jiangsu Key Laboratory of Coast Ocean Resources Development and Environment Security,  
5 Hohai University, Nanjing, China.

6 <sup>2</sup> State Key Laboratory for Estuarine and Coastal Studies, East China Normal University,  
7 Shanghai, China.

8 <sup>3</sup> MOE Key Laboratory for Coast and Island Development, Nanjing University, Nanjing, China.

9 <sup>4</sup> Faculty of Civil Engineering and Geosciences, Delft University of Technology, Delft, the  
10 Netherlands.

11 <sup>5</sup> Deltares, Delft, the Netherlands.

12 Corresponding author: Q. Yu ([qianyu.nju@gmail.com](mailto:qianyu.nju@gmail.com))

### 15 Key Points:

- 16 • Alongshore tidal currents play an important role in cross-shore morphodynamics and  
17 sediment zonation of tidal flats
- 18 • Strong alongshore currents transport sand landward from sub-tidal flat, resulting in sandy  
19 lower flat
- 20 • The upper flat is muddy and convex-up, dominated by cross-shore tidal currents

**Abstract**

Tidal flats, where significant land-ocean interactions take place, are often abstracted as a cross-shore bed profile with sediment zonation from the lower sand flat to the upper mud flat. However, in addition to cross-shore tidal currents, the impact of the alongshore components on cross-shore sediment transport, morphological evolution, and sediment grain-size change remains unclear. Here we investigated the sand-mud tidal flat morphodynamics in the absence of waves by combining approaches of field observations, numerical modeling, and analytical interpretations, based on the example of the tidal flat at the central Jiangsu coast, China. The results show that the morphodynamic processes are complicated by the interactions of cross-shore and alongshore tidal currents, cross-shore flat morphology, and sediment zonation. With identical tidal ranges and increased background alongshore tidal level phase lag, the alongshore currents gradually become dominant at the lower flat, while the upper flat is always dominated by the cross-shore currents. Therefore, in case of different alongshore tidal currents, tidally-dominated bed profiles at the upper flats are quite similar, being convex-up and consist of mud. In contrast, the strong alongshore currents can erode the mud at the lower flat, and promote the landward sand transport from the sub-tidal area to the lower flat, forming a sand flat. The tidally maximum bed shear stress is almost spatially uniform at the muddy area but pronouncedly elevated when the bed sediment coarsens at the lower flat. The contributions of the alongshore tidal currents and sand-mud sorting processes should be adequately addressed in similar coastal environments.

**Plain language summary**

Taken the example of the tidal flat at the central Jiangsu coast, China, we investigated the sand-mud tidal flat morphodynamics by field observations, numerical modeling, and analytical interpretations. We found that the cross- and alongshore tidal currents, cross-shore bed profiles, and sediment zonation interact as a complicated system, in which alongshore tidal currents play an important role in cross-shore morphodynamics. Strong alongshore currents transport sand landward from sub-tidal flat, forming a sandy lower flat, and the tidally maximum bed shear stress becomes much larger than at the muddy upper flat. So we can improve our understanding of the sediment dynamics and morphological evolution of tidal flats under the influence of alongshore tidal currents.

## 52 **1 Introduction**

53 Tidal flats, the transition between subaerial and submarine environments, are areas of  
54 significant land-ocean interactions (Flemming, 2003). They play an important role in material  
55 circulation, coastal protection and ecological conservation (Reise, 2001; Temmerman et al.,  
56 2013). With the accelerated influences of sea-level rise and human activities (e.g. land  
57 reclamation, harbor construction), the studies of tidal flat morphodynamics are crucial to making  
58 comprehensive coastal management strategies (French, 1997; Mangor et al., 2017). Based on  
59 previous observational and modeling works on the tidal flat sediment dynamics (Bartholdy &  
60 Kvale, 2006; Dyer, 2000; Fan, 2012; Flemming & Bartholomä, 1995; Nittrouer et al., 2013), this  
61 study focuses on the alongshore tidal currents impacts on the tidal flat morphodynamics with  
62 emphasis on the sand-mud sorting processes.

63 Cross-shore tidal currents being the main shaping factor, tidal flats are often abstracted as  
64 a one-dimensional cross-shore model in researches on their morphological and sedimentary  
65 characters (Hu et al., 2015; Kirby, 2000; Mariotti & Fagherazzi, 2010; Roberts et al., 2000;  
66 Pritchard & Hogg, 2003; Pritchard et al., 2002). The analytical solutions for equilibrium cross-  
67 shore tidal flat profiles were given by Friedrichs and Aubrey (1996), using the concept of  
68 spatially uniform maximum bed shear stress. The landward residual mud transport and the  
69 consequent cross-shore muddy profile progradation are attributed to spatial and local  
70 asymmetries (Friedrichs, 2011; Hsu et al., 2013; Maan et al., 2015).

71 However, in a number of field settings, the importance of alongshore tidal currents and  
72 related sediment transport processes (Figure 1) were also highlighted (Anderson, 1973; Collins et  
73 al., 1981; Gao, 2009a; Le Hir et al., 2000; Quaresma et al., 2007; Wang et al., 2006; Yang et al.,  
74 2003; Yu et al., 2017; Zhang, 1992). Thus, a quantitative framework is required on the impact of  
75 the alongshore tidal currents on tidal flat hydrodynamics, sediment transport, sediment grain size  
76 and bed level profiles, as well as their feedbacks to the alongshore currents.

77 Tidal flats have a general zonation in sedimentation that the surface sediment gradually  
78 changes from sand at the lower flat to mud at the upper flat (Figure 1) (Amos, 1995; Gao, 2009a).  
79 This general pattern was confirmed at various tidal flats (Alexander et al., 1991; Chang et al.,  
80 2006; Evans, 1965; Frey et al., 1989; Wang & Ke, 1997). The different dynamic processes of  
81 cohesive mud and non-cohesive sand can modify the classical cross-shore mud transport



82 mechanism. The interaction of sand-mud transport, cross-shore equilibrium bed profile, and  
83 sediment zonation is a key issue of the tidal flat morphodynamics. Especially, the existence of  
84 alongshore tidal currents will complicate the interaction, and the related cross-shore sediment  
85 transport mechanisms require further investigation.

86 The objective of this study is to investigate the sand-mud transport processes and the  
87 related morphological responses influenced by alongshore tidal currents, using field observations,  
88 numerical modeling, and primary analytical interpretations. The central Jiangsu coast, China,  
89 which is characterized by strong alongshore tidal currents and sand-mud tidal flat zonation, is a  
90 frequently investigated area of tidal flat sediment dynamics (Gao et al., 2009a, b; Ren et al., 1985;  
91 Wang & Ke, 1997; Yu et al., 2017; Zhang, 1992), and is chosen as the study area. On this basis,  
92 idealized numerical models were utilized to capture the first order characteristics obtained from  
93 observations. Further, the numerical models and analytical solutions help to understand the sand-  
94 mud flat dynamics.

95

## 96 **2 Study Area**

97 The study area is located at the central Jiangsu coast, China, which is situated between  
98 the Changjiang River estuary and abandoned Yellow River mouth (Figure 2a). Tides in this area  
99 are semi-diurnal and meso- to macro-tidal, with a mean tidal range of ca. 4 m (Wang Y.P. et al.,  
100 2012). Because of the southward propagation of the tidal wave, the offshore area is dominated by  
101 alongshore southward flood currents and northward ebb currents. Due to the landward flood and  
102 seaward ebb processes, the cross-shore components are also significant (Yu et al., 2017). The  
103 cross- and alongshore tidal waves are nearly standing, with the alongshore tidal wave relatively  
104 more progressive than the cross-shore tidal wave. The study area is sheltered by a large and  
105 shallow, radial-shaped tidal ridge (or linear sandbank) system (Figure 2a) (Liu et al., 1989; Ren,  
106 1986; Wang Y. et al., 2012), so wave actions are weak. The offshore buoy 20 km north to the  
107 study area (Figure 2a) at the depth of 14 m shows that the annual mean significant wave height is  
108 0.48 m. According to Hayes (1979), this area is tide-dominated.

109 Nowadays, with fine sediments being supplied from the erosion of the abandoned Yellow  
110 River Delta 100 km north to the study area, the coastline here has continued prograding seaward  
111 (Gao, 2009b; Wang Y.P. et al., 2012). The nearshore suspended sediment concentration (SSC) is

112 sufficiently high, and the tidally averaged SSC exceeds  $1 \text{ kg/m}^3$  (Ren, 1986; Wang X.H. et al.,  
113 2011; Yu et al., 2014, 2017). The Dafeng harbor was constructed for freight traffic, in the north  
114 of the study area (Figure 2a). The construction of the sea wall started in early 2007 and finished  
115 in April 2008 (Figure 2b). Due to land reclamation, the intertidal area was all bare and subjected  
116 to a considerable reduction in cross-shore width (Wang Y.P. et al., 2012).

117

### 118 **3 Methods**

119 Firstly, field observations were undertaken across the intertidal flat, including  
120 measurements of sediment dynamics, sampling of water and surface sediment, and repetitive  
121 leveling. Secondly, on these basis schematized models were set up to further study the  
122 coevolution of hydrodynamics, sediment grain size, and morphology.

#### 123 3.1 Field observation

124 Three sets of instruments were deployed across the intertidal flat (along the profile P1) to  
125 measure high-resolution sediment dynamics during May 5 – 12, 2008, just about one year after  
126 the beginning of the seawall construction (Figure 2b). Among them, a YSI/SonTek ADV ocean  
127 with D&A OBS–5+ was deployed on the upper intertidal flat (at station A08) 0.18 m above sea  
128 bed (asb). An observation system was placed at station M08 on the middle intertidal flat, which  
129 has six pairs of electromagnetic current meters and Seapoint turbidity sensors installed 0.38 –  
130 1.12 m asb at Station M08. Further a TRDI WHS 1200 kHz ADCP was installed on a floating  
131 body at station S1 and S3, both near the mean low water level (MLWL). When water depth is  
132 smaller than 1.0 – 1.5 m, the proportion of blanking is too large, therefore effective depth-  
133 averaged velocities cannot be obtained using ADCP. During the measurements, water samples  
134 were collected at various depths to calibrate the OBS–5+ and Seapoint turbidities. High accuracy  
135 measurement of seabed level was undertaken along the profile P1 from the seawall front to the  
136 lower intertidal flat on May 13, 2008, and December 25, 2008, using a Magellan Z-MAX GPS.  
137 Details of the measurements, including SSC calibration statistics, can be found in Wang Y. P. et  
138 al. (2012).

## 139 3.2 Numerical Modeling

### 140 3.2.1 Model Description

141 The two-dimensional, depth-averaged (2DH) version of Delft3D was utilized, including  
142 the Delft3D-FLOW module, the Delft3D bed module for sand-mud mixtures, and the standard  
143 Exner equation for bathymetric evolution via sediment mass conservation (Deltares, 2014;  
144 Lesser, 2004; van Kessel et al., 2012). Two fractions of sediment were considered in the model,  
145 one being cohesive and the other being non-cohesive. Sediment transport of the cohesive and  
146 non-cohesive fractions was computed independently, which was analogous to other modeling  
147 works (Caldwell & Edmonds, 2014; Edmonds & Slingerland, 2010; Geleynse et al., 2011; Rossi  
148 et al., 2016; Tejedor et al., 2016). Erosion and deposition of cohesive sediment were calculated  
149 using the Partheniades-Krone formulations (Partheniades, 1965). The depth-averaged model for  
150 suspended sediment transport based on the asymptotic solution of the convection-diffusion  
151 equation was applied to calculate the erosion and deposition fluxes induced by non-cohesive  
152 sediment transport (Galappatti & Vreugdenhil, 1985; Wang, 1992). Due to the different  
153 dynamics of mixed-size sediments, bed composition is adjusted with the sorting processes  
154 beginning in the active layer. The changes are then progressively transferred to the underlying  
155 layers. Every new bed surface grain-size composition influences the subsequent sorting process,  
156 which eventually results in the change of the total sediment transport rate and bed-level. In this  
157 sense, a multi-layer strata concept was applied in the presence of multi-size sediment fractions.  
158 The “online” approach suggested by Roelvink (2006) was adopted, which speeds up bed  
159 adjustments by multiplying the bed level change in each time step by a morphological scale  
160 factor (MF).

### 161 3.2.2 Model Settings

162 The numerical model is schematized with a rectangular grid and a simple bathymetry  
163 based on the topography of the study area. The model domain is 35 km cross-shore and 20 km  
164 alongshore, consisting of  $200 \times 40$  grid cells. In the cross-shore direction, within 15 km from the  
165 land boundary, the cell size is  $125 \text{ m} \times 500 \text{ m}$ , and the initial bed level decreases from 1 m to -  
166 9.5 m linearly, resulting in a 0.7 ‰ bed slope. The initial bed level starts from 1 m, which is  
167 consistent with the seawall foot’s elevation (land boundary) when it was constructed. In the rest  
168 of 20 km, the grid size is enlarged to  $250 \text{ m} \times 500 \text{ m}$  with uniform initial depth of 9.5m (Figure

169 3). In accordance with the observation, a cross-shore profile (CS) was defined with observation  
170 points O1, O2, and O3 to represent the anchored stations at the upper, middle, and lower  
171 intertidal flat, respectively. The focused area for monitoring the evolution of tidal flat  
172 morphology was also marked in Figure 3.

173 Boundary conditions of water level and sediment concentration are set according to the  
174 field circumstance. The tidal flat is sheltered by the subaerial sand ridges in the east. Because of  
175 the presence of a tidal channel parallel to the coastline, the flow in this region is mainly  
176 alongshore, and water level boundaries are applied only at the north and south edge of the model  
177 domain. According to the observed data (Wang Y.P. et al., 2012) and the validated regional tide  
178 model (Xing et al., 2012), the harmonic constituent  $M_2$  is selected with an amplitude of 2 m, and  
179 the phase lag is defined to 12 degrees from the north to the south boundary. Observations show  
180 the existence of the coastal turbidity maximum at the study area. Suspended sediment (mainly  
181 mud) concentration reaches more than  $1 \text{ kg/m}^3$  at the tidal flat, and decreases quickly to less than  
182  $0.5 \text{ kg/m}^3$  at 20 km offshore (Ren, 1986; Wang X.H. et al., 2011; Xing et al., 2010; Yu et al.,  
183 2014; 2017). Thus, on both boundaries, mud concentration decreases linearly from  $1.25 \text{ kg/m}^3$  at  
184 the landward edge to  $0.25 \text{ kg/m}^3$  at the seaward end, and sand concentration was derived from  
185 equilibrium profiles, which represent the local balance of current shear stress, water depth, and  
186 bed sediment grain size.

187 Both the drying and flooding threshold (Dryflc) and the threshold depth for computing  
188 sediment transport (SedThr) are 0.1 m. A uniform Manning coefficient of  $0.016 \text{ s/m}^{1/3}$  is applied  
189 throughout the whole domain. The grain size of the sand fraction is  $64 \mu\text{m}$ , and the dry bed  
190 density is  $1600 \text{ kg/m}^3$ . The mud parameters are also uniformly defined with settling velocity of  
191  $0.6 \text{ mm/s}$ , critical shear stress for erosion and sedimentation of  $0.15 \text{ Pa}$ , erosion parameter of  
192  $2 \times 10^{-4} \text{ kg/m}^2/\text{s}$ , and dry bed density of  $1000 \text{ kg/m}^3$ . These parameters were selected to represent  
193 the local conditions to a great extent.

194 The initial bed stratigraphy is composed of 5 Lagrangian layers and 45 Eulerian layers,  
195 each 0.2 m thick, and the transport layer is defined to be 0.1 m thick. Bed composition is initially  
196 fully sand. Mud is only supplied from the open boundaries. The morphological scale factor MF  
197 was set to 20 to speed up bed adjustments. The simulation period in the model lasts 111 days,  
198 i.e., covers 6 years.

199 On the basis of the 1<sup>st</sup> year bathymetry and sediment conditions in the morphodynamic  
200 model, a short-term hydrodynamic simulation was carried out. The hydrodynamic and sediment  
201 transport processes can thus be investigated, together with the observed data.

202

## 203 **4 Results**

### 204 4.1 Observational Results

205 Observed cross-shore bed level and sediment grain-size profiles are shown in Figure 4a  
206 and 4c, respectively. The bed level along P1 showed convex-up cross-shore profiles, with an  
207 average slope of ~1.0 ‰. The bed elevation experienced significant accretion from May to  
208 December 2008 (Figure 4a). The accretion thickness ranged from 0.18 m to 0.63 m, with an  
209 average of 0.23 m along the profile. The seabed sediment coarsens seaward, with increasing sand  
210 content up to around 90 % near MLWL. Accompanied by sediment accretion, sand content of  
211 surface sediment mostly decreased along the profile during this period, to an extent of 20 – 40 %,  
212 especially at the middle intertidal flat (Figure 4c).

213 Hydrodynamic observation results are illustrated in Figure 5. Water depth reached up to  
214 about 0.8 m, 2.0 m and 4.0 m at the upper (A08), middle (M08) and lower (S1/S3) intertidal flat,  
215 respectively. The differences in cross-shore current velocities along the intertidal flat profile  
216 were not significant, and the cross-shore velocity components ( $V_c$ ) ranged from -0.35 to 0.23 m/s.  
217 However, the alongshore tidal current speeds ( $V_l$ ) were so different that it was maximally 0.98  
218 m/s at the lower intertidal flat, at most 0.52 m/s at the middle intertidal flat, while nearly zero at  
219 the upper intertidal flat. At the lower intertidal flat (S1/S3),  $V_c$  varied almost symmetrically  
220 during a tidal cycle.  $V_l$  was obviously larger during flood periods, although the flood and ebb  
221 durations (based on the direction of  $V_l$ ) were more or less the same, implying residual currents in  
222 the flood direction.

223 The maximum SSC can be more than 1.5 kg/m<sup>3</sup> at different parts of the intertidal flat  
224 (Figure 5). Due to uncertainties of calibration from ADCP backscatter intensity for high SSC,  
225 SSC at the lower intertidal flat (S1/S3) was not plotted. In most cases, SSC is larger at the middle  
226 flat than at the upper flat.

227

## 228 4.2 Model results

229 The modeled tidal flat morphology can be characterized by cross-shore profile  
230 adjustment and progradation. The alongshore differences in bed elevation of the intertidal flat are  
231 small throughout the modeling period (Figure 6). However, the cross-shore profile experienced  
232 significant accretion from the upper intertidal flat and kept prograding seaward. This character  
233 can be seen more clearly in the evolution of cross-section CS (Figures 6 and 7a). In the vertical  
234 direction, the whole intertidal flat profile accreted, where the upper part was mostly muddy with  
235 accumulation rates up to ca. 0.7 m/yr, and the lower part was mainly sandy with accumulation  
236 rates of more than one order smaller. Sequentially, convex-up tidal flat profiles formed and  
237 prograded seaward. The seaward progradation rate for the elevation of 1 m was ca. 875 m/yr in  
238 the first year, and gradually decreased to ca. 500 m/yr in the second and third year, 375 m/yr in  
239 the fourth and fifth year, and 250 m/yr in the sixth year. The continual progradation patterns  
240 based on symmetric tidal boundaries and waveless scenarios are consistent with other modeling  
241 works (Hu et al., 2015; Le Hir et al., 2007; Maan et al., 2015; Pritchard et al., 2002; Roberts et  
242 al., 2000).

243 The profile at the 4<sup>th</sup> year is regarded as equilibrium in the model. Friedrichs (2011)  
244 defined an equilibrium tidal flat profile loosely as one with a shape that remains more or less  
245 constant over some characteristic period of natural forcing. In the third year the flat began to  
246 accrete up to the mean high water level (MHWL), and afterward, the top elevation kept  
247 prograding seaward. In the 4<sup>th</sup> year, the shape of the tidal flat profile approached a steady state,  
248 when the convex-up profile was fully developed, and thereafter, the maximum bed slope on the  
249 flat is at the MWL.

250 Accompanied by the seaward progradation of the tidal flat, the cross-shore profile of sand  
251 content of surface sediment also moved progressively, indicating that surface sediment grain size  
252 is controlled by the flat elevation (Figure 7b). The upper flat is dominantly mud, while the lower  
253 flat is mostly sand. A mud layer of up to 2.2 m thick was thus preserved in the strata at the  
254 middle intertidal flat due to such progressive patterns of bed level and surface sediment grain  
255 size evolution (Figures 6 and 7a).

256 Figure 8 shows the modeled hydrodynamics during a tidal cycle at the observation points  
257 O1, O2, and O3, which represent the upper, middle and lower intertidal flat, respectively. The

258 maximal water depth at O1, O2, and O3 was 0.8 m, 2.0 m, and 4.0 m, corresponding to an  
259 inundation duration of 2.5, 5.5, and 10 hours. At the upper intertidal flat, the cross-shore current  
260 speed reached up to 0.24 m/s during flood and 0.23 m/s during ebb, while the alongshore tidal  
261 current velocities were nearly zero. Current velocities at the middle intertidal flat were  
262 comparable in both directions, but the cross-shore components were slightly larger: the  
263 maximum flood speed was 0.30 m/s cross-shore and 0.24 m/s alongshore, and the maximum ebb  
264 speed was 0.21 m/s cross-shore and 0.18 m/s alongshore. However, at the lower inter-tidal flat  
265 the alongshore tidal current velocities turned to be stronger, especially during the flood period.  
266 The maximum flood velocity component reached up to 0.48 m/s alongshore and 0.39 m/s cross-  
267 shore. The maximum ebb velocity component alongshore was 0.34 m/s, and 0.38 m/s cross-shore.  
268 Thus, the flood residual currents alongshore were also revealed at the lower flat.

269 The suspended particles were mainly mud, and the concentration of mud was mostly  
270 many orders of magnitude larger than that of sand. The largest mud concentration at O1, O2, and  
271 O3 was 1.3, 1.5, and 1.7 kg/m<sup>3</sup>, respectively. At the upper and middle intertidal flat, the  
272 maximum SSC occurred when the cross-shore current velocities were the largest during the flood  
273 period (i.e. once inundated), while at the lower intertidal flat, the maximum SSC appeared when  
274 the water level is highest or lowest. It is worth noting that resuspension of sand only occurred at  
275 O3 during flood with maximum SSC of 1.4 kg/m<sup>3</sup>, which caused the suspended sand transported  
276 landward and accumulated at the lower intertidal flat. In addition, according to the observed data,  
277 it is assumed that when water depth is smaller than 1.5 m, blanking is too large to get effective  
278 depth-averaged velocities in ADCP measurements. So, the light-yellow zones denote the  
279 estimated ADCP blanking at S1/S3 (Figures 2b and 5).

280

#### 281 4.3 Comparisons between model results and observations

282 Although the schematized models cannot be compared directly with the observations, the  
283 models captured some key patterns and characteristics analogous to the measurements,  
284 concerning spatial variations of bed elevation and composition, hydrodynamics and sediment  
285 transport processes at the three observation points which represent different parts of the intertidal  
286 flat.

287 The modeled bed profiles were close to the observed in configurations. Bed level  
288 measurement along profile P1 (Figure 2b) was firstly undertaken in May 2008 (one year after the  
289 construction of the sea wall), and then in December 2008. To be compared with the observed  
290 data, the modeled bed elevation profile of the cross-section CS at the 1<sup>st</sup> and the 1.6<sup>th</sup> year was  
291 chosen. The selected width of the intertidal flat was also the same as the observations, i.e.,  
292 approximately 3500 m from the land boundary to near MLWL. The modeled bed profile was  
293 also convex-up and kept accreting during the 0.6 years. The accretion thickness ranged from 0.05  
294 m to 0.48 m, with an average of 0.25 m along the profile. These variations were all comparable  
295 with the observations. However, the average bed slope in the model is 0.8 ‰ in the first year and  
296 0.9 ‰ in the 1.6<sup>th</sup> year, which is slightly smaller than the observed profile, indicating the  
297 modeled profile is less convex-up at the meantime (Figures 4a and 4b).

298 The modeled grain size of seabed sediment also coarsens in the seaward direction, with  
299 increasing sand content to 77 % maximally. These patterns were all consistent with the observed  
300 profiles, and in the observation of May 2008, the maximum sand content is around 73 %. Sand  
301 content of surface sediment in the model generally decreased along the profile during this period,  
302 as much as 30 % over the middle intertidal flat. In the observations, sand content decreased most  
303 at the middle intertidal flat to an extent of about 30 % as well (Figures 4c and 4d).

304 Meanwhile, the spatial and temporal variation patterns of modeled current velocities were  
305 also similar to the observations. The three observation points (O1, O2, and O3) were selected  
306 such that maximal water depth and inundation period were all similar to the measurements at the  
307 anchored stations.  $V_c$  changes a little at different parts of the intertidal flat, but  $V_1$  varies a lot at  
308 the three locations both in the model and observations. However,  $V_c$  is slightly larger and  $V_1$  is  
309 obviously smaller in the model (Figures 5 and 8).

310 The slightly larger  $V_c$  is attributed to the smaller modeled bed slope. It is derived from the  
311 continuity equation that  $V_c$  is controlled by the bed slope (Friedrichs & Aubrey, 1996). The  
312 modeled bed slope cross-shore is slightly smaller than observations (Figures 4a and 4b), resulting  
313 in larger  $V_c$ . Besides, ADCP blanking is too large to get effective depth-averaged velocities at  
314 small water depths. The estimated ADCP blanking at the lower intertidal flat (Figure 8) is likely  
315 to cover the maximum  $V_c$ . In other words, the model can obtain the peak values of  $V_c$  which are  
316 probably not measured by ADCP due to large blanking when water depth is small.



317 The smaller  $V_c$  can be interpreted by the differences in tidal range and bed friction.  
 318 Assuming the alongshore water surface slope is uniform, the pressure difference in the  
 319 alongshore direction is balanced by the bed friction in the first order simplification:

$$320 \quad \rho g h s_l = \rho C_D (V_c^2 + V_l^2)^{1/2} V_l \quad (1)$$

321 in which  $\rho$  is water density,  $g$  is the gravitational acceleration,  $h$  is water depth, and  $s_l$  is the  
 322 alongshore water surface slope. The relation of drag coefficient ( $C_D$ ) and manning coefficient ( $n$ )  
 323 is expressed as:

$$324 \quad C_D = g n^2 / h^{1/3} \quad (2)$$

325 Combining equations (1) and (2) yields:

$$326 \quad V_l = S_l h^{4/3} n^{-2} (V_c^2 + V_l^2)^{-1/2} \quad (3)$$

327 On the uppermost flat, where  $V_c \gg V_l$  (e.g., see Figure 5, 8), equation (3) reduces to:

$$328 \quad V_l = S_l h^{4/3} n^{-2} V_c \quad (4)$$

329 while on the lowermost flat, if  $V_l \gg V_c$  (e.g., see Figure 5, 8), equation(3) reduces to:

$$330 \quad V_l = s_l^{1/2} h^{2/3} n^{-1} \quad (5)$$

331 Therefore  $V_l$  increases with both local water depth and the alongshore water slope, while  
 332 inversely proportional to the manning coefficient. The alongshore water surface slope in the  
 333 model is smaller than observations due to a smaller tidal range or alongshore phase lag gradient.  
 334 Furthermore, High SSC causes significant stratification of the water column, and thus induces  
 335 drag reduction, so the drag coefficient or manning coefficient tends to be smaller than that in the  
 336 model. These are all probably why the modeled  $V_l$  is smaller than observed.

337 Both observations and models suggest that tidally induced residual currents flow in the  
 338 flood direction in shallow areas, which is consistent with previous studies (Charlton et al., 1975;  
 339 Friedrichs et al., 1992; Kim et al., 2017; Li & O'Donnell, 1997, 2005; Robinson, 1960;  
 340 Zimmerman, 1974). A nearly standing but slightly progressive tidal wave causes water depth to  
 341 be greater during flood than ebb (Friedrichs et al., 1992). The  $h$  dependence in equation (3) then  
 342 causes  $V_l$  to be stronger on flood in shallow areas where the relative difference in  $h$  between  
 343 flood and ebb is most important. This is seen both in the above references and in the present  
 344 observations and model results. Ebb is enhanced in deep channels in closed-ended tidal

345 embayments because continuity constraints require equal cross-sectionally integrated along-  
346 system transport on ebb and flood. However, there is no such continuity constraint in the open  
347 coast geometry here, so enhanced ebb flow in deeper water is not as relevant. Rather, the  
348 strength of the flood-directed alongshore residual increases as one moves down from the upper  
349 flat into deeper water because the power dependence of  $V_1$  on  $h$  is initially greater than 1. This  
350 means the effect of deeper water on flood driving the residual is increasingly important with  
351 increased water depth. In still deeper water, where  $V_1 \gg V_c$  and the power dependence of  $V_1$  on  $h$   
352 decreases below 1, greater depth causes the strength of the alongshore residual flow to decrease  
353 once more.

354         The model showed respectable consistencies compared to the measured SSCs. In most  
355 cases, SSC decreased landward from the lower flat to the upper flat. The maximum SSC can be  
356 around or even more than  $1.5 \text{ kg/m}^3$  along the intertidal flat. In addition, the maximum SSC was  
357 also associated with the dominant current velocity component. These all agree well with the  
358 observed data (Figures 5 and 8). The slight deviations from the observations, which is mainly  
359 reflected in the temporal variation patterns, is probably because waves were not involved in the  
360 model, they inducing large SSCs in shallow water. It is noted that the observed SSC at the  
361 middle flat (M08) station in Figure 5 often shows two peaks during each tidal cycle,  
362 corresponding to resuspension by maximum velocity both on flood and on ebb. However, the  
363 ebb SSC peak didn't arise in the model (O2 station in Figure 8), which is consistent with the  
364 observed tidal cycles during 0:00 to 6:00 and 12:00 to 18:00, May 10, 2008 (Figure 5). This is  
365 probably because these modeled and the observed tidal cycles are associated with a somewhat  
366 larger asymmetry in alongshore flood versus ebb velocity, producing a greater asymmetry in  
367 suspended resuspension during flood versus ebb.

368

## 369 **5 Discussion**

### 370 **5.1 Impact of alongshore tidal currents**

371         To investigate the influence of alongshore tidal currents, two more cases were set up in  
372 addition to the reference case, in which the phase lag from the north to the south boundary is  $12^\circ$ .  
373 All the other settings keeping the same, but the phase lag changed to  $8^\circ$  and  $16^\circ$ , respectively.

374 The alongshore water level gradient  $s_l$  can be derived as:

$$375 \quad s_l = \frac{d}{dy} [a \cos(\omega t - \varphi)] = a \frac{\partial \varphi}{\partial y} \sin(\omega t - \varphi) \quad (6)$$

376 where  $a$  and  $\omega$  are tidal level amplitude and angular frequency of  $M_2$  tidal current constituent,  
 377 respectively, and  $\varphi$  is the phase in radian.  $V_1$  is proportional to the square root of the alongshore  
 378 water surface slope (equation (5)), and the amplitude of the alongshore water surface slope is  
 379 proportional to the tidal amplitude and alongshore phase gradient (equation (6)). Therefore,  $V_1$   
 380 can be enhanced by increasing the phase lag alongshore.

381 Besides, short-term hydrodynamic simulations were also carried out. Based on the 4<sup>th</sup>  
 382 year bathymetry and hydrodynamic conditions of each case (with a phase lag of 8°, 12°, and 16°),  
 383 when morphology is regarded as approaching equilibrium, hydrodynamic simulations were set  
 384 up with the same phase lag in the morphodynamic model. So the hydrodynamics, sediment and  
 385 morphological characteristics at quasi-equilibrium were investigated among the cases with  
 386 different alongshore phase lags.

387 The 4<sup>th</sup> year bed elevation of the intertidal flat in the other two cases show the same  
 388 characters as the reference case in the alongshore direction (Figure 6). Thus, sensitivity analysis  
 389 only focused differences of the cross-shore profile CS (Figures 9a and 9b). The upper flat is mud  
 390 dominated and had almost the same cross-shore profiles in all cases. At the middle and lower flat,  
 391 the differences between the cases were significant. Here we use sand content of ~25 % as the  
 392 transition between sand dominated and mud dominated (see the dashed lines in grey in Figure 9).  
 393 If the sand content of surface sediment is larger than 25 %, the flat is categorized to mixed and  
 394 sand dominated (hereinafter called ‘sand flat’ in short); while the flat with sand content lower  
 395 than 25% is regarded as ‘mud flat’.

396 Sand flat expands landward when the phase lag increases. In case 1 (red curve) with a  
 397 phase lag of 8°, the whole intertidal flat was mainly composed of mud, and the bed profile is  
 398 almost a uniform slope of ~0.8 ‰. However, in case 2 (black curve, with phase lag of 12°), the  
 399 lower flat is sandy and the mean bed slope is ~0.7 ‰, and in case 3 (blue curve, with phase lag  
 400 of 16°), the sand flat even expands from the lower flat to the middle flat with a smaller mean  
 401 slope of ~0.5 ‰. The bed slope of the transition zone between the mud and sand flat is much  
 402 steeper: ~1.6 ‰ in case 2 and ~1.7 ‰ in case 3 (Figures 9a and 9b).

403 Short-term hydrodynamics based on the 4<sup>th</sup> year morphology (equilibrium tidal flat  
404 profiles) in the three cases were also compared. According to equations (5) and (6), the  
405 alongshore tidal currents are positively related to water depth and alongshore phase lag, and the  
406 former has a larger impact. Therefore, on the mud flat where the bed profiles and water depths  
407 are very close,  $V_1$  is mainly controlled by alongshore phase lag, and is largest in the 16° case,  
408 smallest in the 8° case. However, bed shear stress and morphodynamics on the upper mud flat in  
409 all three cases are controlled more by  $V_c$ , because  $V_c$  is much larger than  $V_1$  there. On the sand  
410 flat where the bed profiles vary a lot,  $V_1$  is mainly controlled by water depth. Accordingly, the 12°  
411 case has the largest  $V_1$  then (Figure 9c).  $V_c$  is controlled by the cross-shore bed slope, and thus  
412 have little difference on the mud flat. But on the sand flat, the 16° case has the largest  $V_c$  induced  
413 by the mildest bed slope (Figure 9d). On the sand flat,  $V_1$  and  $V_c$  are both important to bottom  
414 shear stress and morphodynamics because of similar magnitudes, and in some areas,  $V_1$  is even  
415 larger than  $V_c$ .

416 The dynamic equilibrium theory of tidal flat is used to interpret the model results. It  
417 assumes that morphological equilibrium is associated with spatially uniform tidally maximum  
418 bed shear stress ( $\tau_{\max}$ ) (Friedrichs, 2011). If the flat profile is static,  $\tau_{\max}$  is equal to the critical  
419 bed shear stress (Friedrichs & Aubrey, 1996). This theory has been supported by many  
420 observational and modeling studies (Bearman et al., 2010; Chen et al., 2010; Hu et al., 2015; Hsu  
421 et al., 2013; Kirby, 2000; Pritchard & Hogg, 2003; Pritchard et al., 2002; van der Wegen & Jaffe,  
422 2014).

423 In this study, the modeled upper flat has steady shapes and the flat profiles kept  
424 prograding seaward. Such uniform distributions of  $\tau_{\max}$  also exist on the mud flat and the values  
425 are almost the same in the three cases with different alongshore phase lags. This agrees with the  
426 above researches. However, the mean value of the uniformly distributed  $\tau_{\max}$  on the mud flat is ca.  
427 0.3 Pa, which is twice of the critical shear stress of mud (0.15 pa) in the model (Figure 9e). This  
428 is probably because the high SSC results in large deposition rates, and the uniform  $\tau_{\max}$  has to be  
429 enhanced so as to balance the deposition (Friedrichs, 2011; Hu et al., 2015).

430 Meanwhile, on the sand flat in the 12° and 16° cases,  $\tau_{\max}$  are greatly enhanced up to ~1.0  
431 Pa and spatially varying. The dashed arrows indicate the turning points of  $\tau_{\max}$  in these two cases,  
432 which are both corresponding to the transitions between mud and sand flat (Figure 9a, e).

433 Possible interpretations are proposed. Firstly, only a single sediment fraction was taken into  
434 account in the dynamic equilibrium theory, while two fractions (a mud fraction and a sand  
435 fraction) were involved in our models. The spatial variations of sediment grain size lead to  
436 different dynamic properties, relating to different  $\tau_{\max}$ . Secondly, at the 4<sup>th</sup> year in the models, the  
437 shape of mud flat profiles was steady but the sand flat profiles were still changing. Therefore the  
438 uniform  $\tau_{\max}$  on the sand flats does not exist.

439 Furthermore, responses of hydrodynamics, sediment transport and morphology to the  
440 variation of  $V_l$  were also studied. Starting from the 1st year bathymetry and sediment conditions  
441 of the reference case (see the cross-shore profiles of intertidal flat in Figure 4b, d), short-term  
442 hydrodynamic simulations were undertaken with the alongshore phase lag of 8°, 12° and 16°,  
443 respectively. Equations (5) and (6) show that the alongshore tidal current is enhanced with  
444 increasing phase lag (Figure 10a). Due to the identical cross-shore bed slope, the cross-shore  
445 tidally maximum flood current speeds exhibit little difference with changing alongshore phase  
446 lag (Figure 10b). In response to such hydrodynamic conditions, the tidally averaged SSC of mud  
447 and sand were also increased by the enhancement of alongshore tidal currents (Figures 10c and  
448 10d). Sand concentration is 0 at the upper and middle flat and quickly increases from lower flat  
449 to sub-flat area. The maximum tidally-averaged SSC of sand in the 16° case is up to 0.002 kg/m<sup>3</sup>,  
450 which is 8 times that of the 12° case, and 1400 times of the 8° case.

451 During flood, the strong alongshore tidal currents (the 16° case) at the lower flat cause  
452 resuspension of mud, and the cross-shore tidal currents bring it onshore where it then settled due  
453 to weakening current speed. Mud thus accreted on the upper intertidal flat, while mud eroded and  
454 left relict sand at the lower part, shaping a steeper cross-shore bed profile (Figure 10e). Likewise,  
455 sand can also be resuspended by increased alongshore tidal currents mainly from the subtidal-flat  
456 (Figure 10d) and accumulated on the lower intertidal flat (Figure 10f). The area where sands  
457 accumulated corresponds to where mud was eroded (Figures 10e and 10f). These morphological  
458 and sedimentological responses explain the cross-shore profiles of bed elevation and sand  
459 content at the quasi-equilibrium states (Figures 9a and 9b).

460 In the 8° case with relatively weak alongshore tidal currents, mud accumulated across the  
461 whole intertidal flat, and at the lower flat, the deposition rate increased seaward (Figure 10e),  
462 resulting in a milder cross-shore bed slope and an increase of mud content at lower flat. There

463 was no suspended sand across the whole flat and the sand deposition rates were all zero, so the  
 464 intertidal flat tend to be fully muddy (Figure 10f). These trends were also confirmed in Figures  
 465 9a and 9b.

466

## 467 5.2 Mechanisms of landward sand transport

468 A two-dimensional (both cross-shore and alongshore tidal currents included) analytical  
 469 solution was obtained to express the tidal residual sand transport. The mechanisms of the  
 470 landward sand transport can thus be further analyzed.

471 In the nearshore shallow area of the present model (Figure 3), due to the homogeneous  
 472 bathymetry alongshore, the cross-shore (X direction) residual tidal current is zero. But the  
 473 alongshore (Y direction) residual tidal current exists. Current velocities in X and Y directions  
 474 can be expressed as follows. Assuming that the amplitude of  $M_2$  tidal constituent dominates the  
 475 current velocity,  $\varepsilon_{U_i}$  and  $\varepsilon_{V_i}$  are in the order of  $10^{-1}$ .

476 Velocity in X direction:

$$\begin{aligned}
 U(t) &= U_2 \cos(\omega t - \phi_{U_2}) + U_4 \cos(2\omega t - \phi_{U_4}) \\
 &= U_2 [\cos(\omega t - \phi_{U_2}) + \varepsilon_{U_4} \cos(2\omega t - \phi_{U_4})]
 \end{aligned}
 \tag{7}$$

478 Velocity in Y direction:

$$\begin{aligned}
 V(t) &= V_0 + V_2 \cos(\omega t - \phi_{V_2}) + V_4 \cos(2\omega t - \phi_{V_4}) \\
 &= V_2 [\varepsilon_{V_0} + \cos(\omega t - \phi_{V_2}) + \varepsilon_{V_4} \cos(2\omega t - \phi_{V_4})]
 \end{aligned}
 \tag{8}$$

480 in which:

481  $V_0$  = residual current in Y direction;

482  $\omega$  = angular frequency of  $M_2$  tidal current constituent;

483  $U_i$  = amplitude of the other tidal current constituent in X direction, e.g.  $U_2$  is related to  
 484  $M_2$  constituent, and  $U_4$  corresponds to  $M_4$ ;

485  $V_i$  = amplitude of the other tidal current constituent in Y direction;

486  $\phi_{U_i}$  = phase of tidal constituent  $M_i$  in X direction;

487  $\phi_{V_i}$  = phase of tidal constituent  $M_i$  in Y direction;

$$488 \quad \varepsilon_{U_i} = \frac{U_i}{U_2} \quad (i = 4);$$

$$489 \quad \varepsilon_{V_i} = \frac{V_i}{V_2} \quad (i = 0 \text{ or } 4)$$

490 mm/s for 64  $\mu\text{m}$  sand, the phase lag of sand concentration to velocity is relatively small (Yu et al.,  
491 2011, 2012), suggesting the approximately local balance of suspended sand and tidal current  
492 shear stress. According to Friedrichs and Aubrey (1988), Gräwe et al. (2014) and Olaberrieta et  
493 al. (2018), instantaneous sand transport rate is proportional to cubic of current velocity. Thus, the  
494 residual transport rate of non-cohesive sediment (sand) during an  $M_2$  period in the X direction is:

$$\bar{q}_x = \frac{1}{T} \int_0^T q_x(t) dt$$

$$495 \quad q_x(t) = k(U(t)^2 + V(t)^2)U(t) \quad (9)$$

496 where  $T$  is the  $M_2$  tidal period,  $k$  is a constant.

497 By omitting the small quantities of third order ( $O(\epsilon^3)$ ), it is derived:

$$\frac{\bar{q}_x}{kU_2^3} = A + B + C$$

$$A = \varepsilon_{v_0} \alpha^2 \cos(\phi_{U_2} - \phi_{V_2})$$

$$B = \frac{1}{4} \varepsilon_{U_4} [3 \cos(2\phi_{U_2} - \phi_{U_4}) + \alpha^2 \cos(2\phi_{V_2} - \phi_{U_4})]$$

$$C = \frac{1}{2} \varepsilon_{V_4} \alpha^2 \cos(\phi_{U_2} + \phi_{V_2} - \phi_{V_4})$$

$$498 \quad \alpha = V_2/U_2 \quad (10)$$

499 In the present study area where slightly progressive  $M_2$  tidal waves prograde southward  
500 (in the alongshore direction), the phases of  $M_2$  constituent in X and Y directions are close  
501 nearshore, which is supported by the observed and modeled hydrodynamics (Figure 5, 8), and  
502 also the harmonic analysis results of tidal velocities measured at a sub-tidal station near the study  
503 area (cf. Supporting information). Thus it is assumed that  $\phi_{U_2} = \phi_{V_2} = \phi_2$ , and the above  
504 equations can be further simplified as:

$$A = \frac{3}{2} \varepsilon_{v_0} \alpha^2$$

$$B = \frac{1}{4} \varepsilon_{U_4} (3 + \alpha^2) \cos(2\phi_2 - \phi_{U_4})$$

$$C = \frac{1}{2} \varepsilon_{V4} \alpha^2 \cos(2\phi_2 - \phi_{V4}) \quad (11)$$

Therefore, the residual sand transport in X (cross-shore) direction ( $\overline{q_x}$ ) is scaled by 3<sup>th</sup> power of  $U_2$ .  $A$ ,  $B$ , and  $C$  are non-dimensional terms, and their analytical expressions reveal the mechanisms of the cross-shore residual sand transport.

Term  $A$  is residual current related, the direction of which is controlled by Y residual current, and magnitude is proportional to the magnitude of the Y residual current and the ratio of the  $M_2$  tidal current amplitude in Y direction to X direction ( $\alpha$ ). It is then suggested that negative Y (southward (flood) direction in the present model) residual currents generate negative X (westward (flood) direction in the present model) residual sand transport, and the strong Y  $M_2$  tidal amplitude enlarges  $\alpha$ , so as to enhance the magnitude of  $A$ . Both observations and modeling indicated that when the alongshore phase lag is large (e.g. the 16° case), the alongshore residual currents are southward ((flood) “–”) and the  $\alpha$  value is quite large at the lower and sub-tidal flat, the landward sand transport is thus induced. In case of the Jiangsu Coast, the observations at a sub-tidal station near the study area (cf. Supporting information) also show the strong alongshore residual currents in the flood direction and a large  $\alpha$  value.

Term  $B$  and  $C$  are related to tidal asymmetry in X (cross-shore) and Y (alongshore) direction, respectively. The  $M_4$  currents are not only in X direction but also Y direction and contribute to the cross-shore residual sand transport. The phase lag of  $(2\phi_2 - \phi_{U4})$  and  $(2\phi_2 - \phi_{V4})$  determine their directions, and the relative amplitude of  $M_4$  currents ( $\varepsilon_{U4}$  and  $\varepsilon_{V4}$ ) and  $\alpha$  control the magnitudes. In the shallow areas, the larger ratio of tidal amplitude to water depth promotes flood-dominant tidal asymmetries (Friedrichs et al., 1992). Because both the positive X and Y are ebb directions, flood-dominant tidal asymmetries correspond to the 90° to 270° phase lag of  $(2\phi_2 - \phi_{U4})$  and  $(2\phi_2 - \phi_{V4})$ . Thus, terms  $B$  and  $C$  are negative, indicating westward/landward residual sand transport.

It is worth noting that the relative importance of the Y (alongshore) tidal currents (represented by  $\alpha$ ) is crucial to the sum of  $A$ ,  $B$ , and  $C$ . If  $\alpha$  is sufficiently smaller than 1, term  $A$  and  $C$  will reduce to a small value and term  $B = \frac{3}{4} \varepsilon_{U4} \cos(2\phi_2 - \phi_{U4})$ , suggesting that the X (cross-shore) residual sand transport is then only caused by the cross-shore tidal asymmetry. However, if  $\alpha$  is sufficiently larger than 1, like the observations at the lower flat station (Figure 5)



534 the above part of X (cross-shore) tidal asymmetry (i.e.  $\frac{3}{4}\varepsilon_{U4} \cos(2\phi_2 - \phi_{U4})$ ) will only account  
 535 for a small fraction of term  $B$ , and all three terms ( $A$ ,  $B$ , and  $C$ ) will be controlled by  $\alpha^2$ .

536 According to equations (5) and (6), under the same bathymetry in the present model, the  
 537 alongshore tidal currents increase proportionally to the square root of the alongshore phase lag  
 538 (Figure 10a). But the consequent X (cross-shore) residual sand transport will increase much more  
 539 quickly (equation (11)). This partly explains the mechanisms of the landward sand transport and  
 540 the sandy lower flat formation, which are induced by the strong alongshore tidal currents.

541 In contrast, if slightly progressive  $M_2$  tidal waves prograde northward, the  $M_2$  phase in X  
 542 direction deviates  $\sim 180^\circ$  from Y direction ( $\phi_{U2} + \pi = \phi_{V2}$ ).

$$A = -\frac{3}{2}\varepsilon_{v0}\alpha^2$$

$$B = \frac{1}{4}\varepsilon_{U4}(3 + \alpha^2) \cos(2\phi_{U2} - \phi_{U4})$$

$$543 \quad C = -\frac{1}{2}\varepsilon_{V4}\alpha^2 \cos(2\phi_{V2} - \phi_{V4}) \quad (12)$$

544 Similarly, the northward (positive) residual current velocity results in the negative  
 545 (westward/landward)  $A$ . Terms  $B$  and  $C$  are also controlled by the tidal asymmetry. The positive  
 546 X and Y are associated with the ebb and the flood direction, respectively. Flood-dominant tidal  
 547 asymmetries correspond to the  $90^\circ$  to  $270^\circ$  phase lag of  $(2\phi_{U2} - \phi_{U4})$  and the  $-90^\circ$  to  $90^\circ$  phase  
 548 lag of  $(2\phi_{V2} - \phi_{V4})$ , suggesting westward/landward residual sand transport as well due to  
 549 negative terms of  $B$  and  $C$ . Numerical models also show that tidal flat morphology and sediment  
 550 zonation are not influenced by a reversed direction of tidal wave propagation.

551 The above cases are associated with an only slightly progressive  $M_2$  constituent in the  
 552 alongshore direction. However, due to a large scale and low frictions in the alongshore direction  
 553 and a small scale in the cross-shore direction, it is worth considering a case where the alongshore  
 554 tidal wave is purely progressive and the cross-shore tidal wave is purely standing. In this case,  
 555  $\phi_{U2} = \phi_{V2} - \frac{\pi}{2}$ , and then equation (10) can be simplified as:

$$A = 0$$

$$B = \frac{1}{4}\varepsilon_{U4}(3 - \alpha^2) \cos(2\phi_{U2} - \phi_{U4})$$

$$C = \frac{1}{2} \varepsilon_{V4} \alpha^2 \sin(2\phi_{V2} - \phi_{V4}) \quad (13)$$

557 The above solution suggests that if the alongshore and cross-shore tidal velocities are 90  
 558 degrees out of phase, the alongshore residual currents are irrelevant to the cross-shore residual  
 559 sand transport ( $A = 0$ ). Without the presence of the alongshore tidal velocities ( $\alpha = 0$ ), term  $B$  is  
 560 controlled by the peak velocity asymmetry in the cross-shore direction ( $\cos(2\phi_{U2} - \phi_{U4})$ ).  
 561 However, the amplified alongshore  $M_2$  tidal velocity amplitude can reduce the term  $B$ , and the  
 562 large  $\alpha$  can even change the direction of term  $B$ . The direction of term  $C$  is controlled by  
 563  $\sin(2\phi_{V2} - \phi_{V4})$ , which represents the slack water duration asymmetry rather than the peak  
 564 velocity asymmetry in the alongshore direction. The most flood-dominated alongshore tidal  
 565 currents with  $2\phi_{V2} - \phi_{V4}$  of  $0^\circ$ , which means term  $C$  equals to zero, can not result in cross-  
 566 shore residual sand transport. This is pronouncedly different from the above cases.

567

### 568 5.3 Future works

569 This study is based on the case of Jiangsu coast, China, and the role of alongshore tidal  
 570 currents on sand/mud transport and tidal flat morphodynamics was investigated. However, for a  
 571 comprehensive understanding, more field examples and sensitivity analysis are required with  
 572 different settings, such as tidal range, alongshore tidal properties (standing to progressive), initial  
 573 bed profile, boundary sand and mud concentrations, etc. The analytical solution helps to  
 574 understand the cross-shore transport of sand, however, similar two-dimensional solutions of the  
 575 cross-shore transport of mud are more complicated due to the temporal and spatial settling lags  
 576 and their effects on horizontal advection. It could be developed based on one-dimensional  
 577 solutions (Yu et al., 2012).

578 Observational (Andersen et al., 2006; Christiansen, 2006; Deloffre et al., 2005, 2007; Fan  
 579 et al., 2006; Marion et al., 2009; Shi et al., 2017; Wang et al., 2009; Yang et al., 2003, 2008) and  
 580 modeling (Fagherazzi, et al, 2007; Hu et al., 2015; Maan et al., 2015; Roberts et al., 2000) works  
 581 both revealed that waves have important impacts on the morphology and sediment grain size of  
 582 tidal flats. So future research should couple the effects of cross-shore and alongshore tidal  
 583 currents, as well as waves.

584 Here we only considered one mud fraction and one sand fraction in the models. In fact,  
585 both sand and mud can be divided into more fractions of different properties. Models using more  
586 sediment fractions would provide more details regarding the processes of sediment transport and  
587 morphological evolution, especially at the transitions between the mud flat and sand flat (Chou et  
588 al., 2018; Guillou et al., 2009; van der Wegen & Jaffe, 2014; Wang et al., 2014, 2016).

589 Sediment transport of sand and mud was calculated separately. However, interactions  
590 exist between sand and mud. If it is taken into account in the erosion formulae, a distinction is  
591 made when the mud content remains below a critical value, the regime is non-cohesive, and  
592 otherwise, it switches to cohesive (van Ledden et al., 2004; van Rijn, 2007). Models with sand-  
593 mud interactions were suggested, and the performance of this method needs further evaluation  
594 (Braat et al., 2017; Carniello et al., 2012; Dufois et al., 2014; Le Hir et al., 2011; Paarlberg et al.,  
595 2005; Ulses et al., 2008; van Ledden et al., 2006).

596 During the observation periods, the whole intertidal flat was bare. Thus the role of  
597 biological processes and salt marshes were not considered in the models. But marshes may  
598 colonize the upper flat and expand over time. It is then necessary to observe and simulate the  
599 biomorphodynamic processes of intertidal flats, which were discussed by a number of studies  
600 (D'Alpaos et al., 2007; Fagherazzi et al., 2012; Kirwan & Murray, 2007; Marani et al., 2010;  
601 Mariotti & Fagherazzi, 2010; Mudd et al., 2010; Schwarz et al., 2014; Tambroni & Seminara,  
602 2012).

603

## 604 **6 Conclusions**

605 In addition to cross-shore tidal currents, the alongshore components also play an  
606 important role in sediment transport, morphological evolution, and sediment grain-size change in  
607 the cross-shore direction of the tidal flat. With an increase in the background alongshore tidal  
608 water level phase lag, the alongshore currents are gradually dominant on the lower flat. In  
609 contrast, the upper flat is always dominated by cross-shore currents, which are controlled by the  
610 cross-shore bed profile. Thus, in case of different alongshore tidal currents, bed profiles at the  
611 upper flats are quite similar, being convex-up and consist of mud. However, strong alongshore  
612 currents can erode the mud at the lower flat, and promote the landward sand transport from the  
613 subtidal area to the lower flat, forming a sand flat. The tidally maximum bed shear stress is

614 almost spatially uniform across the muddy area of the cross-shore profile, but bed stresses are  
 615 pronouncedly elevated when the bed sediment coarsens at the lower flat.

## 616 **Acknowledgments**

617 We thank Jia Jianjun, Gao Jianhua, Yang Yang, Du Xiaoqin, Xing Fei, Li Jiasheng, Liu  
 618 Yunling, Cheng Jun, Wang Huaqiang, and Ran Qi for participating in the field work. We thank  
 619 Li Runxiang for modifying Figure 2. This study is supported by the National Natural Science  
 620 Foundation of China (41676077, 41676081), and the Fundamental Research Funds for the  
 621 Central Universities (2016B00814). Y.P. Wang acknowledges the funding from the National  
 622 Natural Science Foundation of China (41625021). Data in support of this manuscript are  
 623 available at <https://figshare.com/projects/2018JC014550/60053#>. We highly acknowledge Carl  
 624 Friedrichs and an anonymous reviewer for their constructive and valuable suggestions that  
 625 allowed for an improvement of the quality of the manuscript.

626

## 627 **References**

- 628 Alexander C. R., Nittrouer, C. A., DeMaster, D. J., Park, Y.-A., & Park, S.-C. (1991). Macrotidal  
 629 mudflats of west Korea: a model for interpretation of intertidal deposits. *Journal of Sedimentary*  
 630 *Research*, 61(5), 805–824. <https://doi.org/10.1306/D42677DA-2B26-11D7-8648000102C1865D>
- 631 Amos, C. L. (1995). Siliclastic tidal flats. In G. M. E. Perillo (Ed), *Geomorphology and sedimentology of*  
 632 *estuaries* (pp. 273–306). Amsterdam: Elsevier.
- 633 Andersen, T. J., Pejrup, M., & Nielsen, A. A. (2006). Long-term and high-resolution measurements of  
 634 bed level changes in a temperate, microtidal coastal lagoon. *Marine Geology*, 226, 115–125.  
 635 doi:10.1016/j.margeo.2005.09.016
- 636 Anderson, F.E. (1973). Observations of some sedimentary processes acting on a tidal flat. *Marine*  
 637 *Geology*, 14(2), 101–116. [https://doi.org/10.1016/0025-3227\(73\)90054-6](https://doi.org/10.1016/0025-3227(73)90054-6)
- 638 Bartholdy, J., & Kvale, E. P. (2006). Introduction to proceedings from 6th international conference on  
 639 tidal sedimentology. *Marine Geology*, 235, 1–4. doi: 10.1016/j.margeo.2006.10.024
- 640 Bearman, J. A., Friedrichs, C. T., Jaffe, B. E., & Foxgrover, A. C. (2010). Spatial trends in tidal flat shape  
 641 and associated environmental parameters in South San Francisco Bay. *Journal of Coastal Research*,  
 642 26(2), 342–349. <https://doi.org/10.2112/08-1094.1>

- 643 Braat, L., van Kessel, T., Leuven, J. R. F. W., & Kleinhans, M. G. (2017). Effects of mud supply on  
644 large-scale estuary morphology and development over centuries to millennia. *Earth Surface*  
645 *Dynamics*, 5, 617–652. doi:10.5194/esurf-5-617-2017
- 646 Caldwell, R. L., & Edmonds, D. A. (2014). The effects of sediment properties on deltaic processes and  
647 morphologies: A numerical modeling study. *Journal of Geophysical Research: Earth Surface*, 119,  
648 961–982. doi:10.1002/2013JF002965
- 649 Carniello, L., Defina, A., & D’Alpaos, L. (2012). Modeling sand-mud transport induced by tidal currents  
650 and wind waves in shallow microtidal basins: Application to the Venice Lagoon (Italy). *Estuarine,*  
651 *Coastal and Shelf Science*, 102–103, 105–115. <http://dx.doi.org/10.1016/j.ecss.2012.03.016>
- 652 Chang, T.S., Bartholomä, A., & Flemming, B.W. (2006). Seasonal dynamics of fine-grained sediments in  
653 a back-barrier tidal basin of the German Wadden Sea (southern North Sea). *Journal of Coastal*  
654 *Research*, 22(2), 328–338. doi:10.2112/03-0085.1
- 655 Charlton, J. A., McNicoll, W., & West, J. R. (1975). Tidal and freshwater induced circulation in the Tay  
656 Estuary. *Proceedings of the Royal Society of Edinburgh, Section B: Biological Sciences*, 75(1–2),  
657 11–27. doi:10.1017/S0308211300002504
- 658 Chen, S.-N., Geyer, W. R., Sherwood, C. R., & Ralston, D. K. (2010). Sediment transport and deposition  
659 on a river dominated tidal flat: An idealized model study. *Journal of Geophysical Research*, 115,  
660 C10040. doi:10.1029/2010JC006248
- 661 Chou, Y. - J., Nelson, K. S., Holleman, R. C., Fringer, O. B., Stacey, M. T., Lacy, J. R., et al. (2018).  
662 Three - dimensional modeling of fine sediment transport by waves and currents in a shallow estuary.  
663 *Journal of Geophysical Research: Oceans*, 123, 4177–4199. <https://doi.org/10.1029/2017JC013064>
- 664 Christiansen, C., Vølund, G., Lund-Hansen, L.C., & Bartholdy, J. (2006). Wind influence on tidal flat  
665 sediment dynamics: Field investigations in the Ho Bugt, Danish Wadden Sea. *Marine Geology*,  
666 235(1–4), 75–86. <https://doi.org/10.1016/j.margeo.2006.10.006>
- 667 Collins, M. B., Amos, C. L., & Evans, G. (1981). Observations of some sediment - transport processes  
668 over intertidal flats, the Wash, U.K.. In S. Nio, R.T. Shüttenhelm, T.C. Van Weering (Eds.),  
669 *Holocene marine sedimentation in the North Sea basin*. doi:10.1002/9781444303759.ch6
- 670 D’Alpaos, A., Lanzoni, S., Marani, M., & Rinaldo, A. (2007). Landscape evolution in tidal embayments:  
671 Modeling the interplay of erosion, sedimentation, and vegetation dynamics. *Journal of Geophysical*  
672 *Research*, 112, F01008. doi:10.1029/2006JF000537

- 673 Deloffre, J., Lafite, R., Lesueur, P., Lesourd, S., Verney, R., & Gue'zennec, L. (2005). Sedimentary  
674 processes on an intertidal mudflat in the upper macrotidal Seine estuary, France. *Estuarine, Coastal  
675 and Shelf Science*, 64, 710–720. <https://doi.org/10.1016/j.ecss.2005.04.004>
- 676 Deloffre, J., Verney, R., Lafite, R., Lesueur, P., Lesourd, S., & Cundy, A. (2007). Sedimentation on  
677 intertidal mudflats in the lower part of macrotidal estuaries: Sedimentation rhythms and their  
678 preservation. *Marine Geology*, 241, 19–32. doi:10.1016/j.margeo.2007.02.011
- 679 Deltares (2014). *Delft3D-FLOW, Simulation of multi-dimensional hydrodynamic flows and transport  
680 phenomena, including sediments, User manual* (version: 3.15.34158). Retrieved from  
681 [https://oss.deltares.nl/documents/183920/185723/Delft3D-FLOW\\_User\\_Manual.pdf](https://oss.deltares.nl/documents/183920/185723/Delft3D-FLOW_User_Manual.pdf)
- 682 Dufois, F., Verney, R., Le Hir, P., Dumas, F., & Charmasson, S. (2014). Impact of winter storms on  
683 sediment erosion in the Rhone River prodelta and fate of sediment in the Gulf of Lions (North  
684 Western Mediterranean Sea). *Continental Shelf Research*, 72, 57–72.  
685 <https://doi.org/10.1016/j.csr.2013.11.004>
- 686 Dyer, K. R. (2000). Preface. *Continental Shelf Research*, 20, 1037–1038. [https://doi.org/10.1016/S0278-  
4343\(00\)00010-8](https://doi.org/10.1016/S0278-<br/>687 4343(00)00010-8)
- 688 Edmonds, D. A., & Slingerland, R. L. (2010). Significant effect of sediment cohesion on delta  
689 morphology. *Nature Geoscience*, 3(2), 105–109. doi:10.1038/NGEO730
- 690 Englund, F., & Hansen E. (1967). *A monograph on sediment transport in alluvial streams*. Copenhagen:  
691 Teknisk Forlag.
- 692 Evans, G. (1965). Intertidal flat sediments and their environments of deposition in the Wash. *Quarterly  
693 Journal of the Geological Society*, 121, 209–240. <http://dx.doi.org/10.1144/gsjgs.121.1.0209>
- 694 Fagherazzi, S., Kirwan, M. L., Mudd, S. M., Guntenspergen, G. R., Temmerman, S., D'Alpaos, A., et al.  
695 (2012). Numerical models of salt marsh evolution: Ecological, geomorphic, and climatic factors.  
696 *Reviews of Geophysics*, 50, RG1002, doi:10.1029/2011RG000359
- 697 Fagherazzi, S., Palermo, C., Rulli, M. C., Carniello, L., & Defina, A. (2007). Wind waves in shallow  
698 microtidal basins and the dynamic equilibrium of tidal flats. *Journal of Geophysical Research*, 112,  
699 F0204. doi:10.1029/2006JF000572
- 700 Fan, D. (2012). Open-coast tidal flats. In R.A. Davis, Jr., R.W. Dalrymple (Eds.), *Principles of tidal  
701 sedimentology* (pp. 187–229). Dordrecht: Springer.

- 702 Fan, D., Guo, Y., Wang, P., & Shi, J. Z. (2006). Cross-shore variations in morphodynamic processes of  
703 an open-coast mudflat in the Changjiang Delta, China: With an emphasis on storm impacts.  
704 *Continental Shelf Research*, 26, 517–538. doi:10.1016/j.csr.2005.12.011
- 705 Flemming, B. W. (2003). Tidal flats. In G. V. Middleton (Ed.), *Encyclopedia of sediments and*  
706 *sedimentary rocks* (pp. 734–737). Dordrecht: Kluwer.
- 707 Flemming, B. W., & Bartholomä, A. (Eds.) (1995). *Tidal signatures in modern and ancient sediments*  
708 (IAS Special Publication No. 24). Oxford: Blackwell Science. doi:10.1002/9781444304138
- 709 French, P. (1997). *Coastal and estuarine management*. London: Routledge.  
710 <https://doi.org/10.4324/9780203437278>
- 711 Frey, R. W., Howard, J. D., Han, S.-J., & Park, B.-K. (1989). Sediments and sedimentary sequences on a  
712 modern macrotidal flat, Inchon, Korea. *Journal of Sedimentary Research*, 59(1), 28–44.  
713 <https://doi.org/10.1306/212F8F0D-2B24-11D7-8648000102C1865D>
- 714 Friedrichs, C. T. (2011). Tidal flat morphodynamics: A synthesis. In E. Wolanski, D. McLusky (Eds.),  
715 *Treatise on estuarine and coastal science* (pp. 137–170). Waltham: Academic Press.
- 716 Friedrichs, C. T., & Aubrey, D. G. (1988). Non-linear tidal distortion in shallow well mixed estuaries: A  
717 synthesis. *Estuarine, Coastal and Shelf Science*, 27(5), 521–545. [https://doi.org/10.1016/0272-](https://doi.org/10.1016/0272-7714(88)90082-0)  
718 [7714\(88\)90082-0](https://doi.org/10.1016/0272-7714(88)90082-0)
- 719 Friedrichs, C. T., & Aubrey, D. G. (1996). Uniform bottom shear stress and equilibrium hypsometry of  
720 intertidal flats. In C. Pattiaratchi (Ed), *Coastal and estuarine studies* (Vol. 50, pp. 405–429).  
721 Washington, DC: American Geophysical Union.
- 722 Friedrichs, C. T., Lynch, D. R., & Aubrey, D. G. (1992). Velocity asymmetries in frictionally-dominated  
723 tidal embayments: Longitudinal and lateral variability. In D. Prandle (Ed), *Dynamics and exchanges*  
724 *in estuaries and the coastal zone* (Vol. 40, pp. 277–312). American Geophysical Union.  
725 <https://doi.org/10.1029/CE040p0277>
- 726 Galappatti, G., & Vreugdenhil, C. B. (1985). A depth-integrated model for suspended sediment transport.  
727 *Journal of Hydraulic Research*, 23(4), 359–377. <https://doi.org/10.1080/00221688509499345>
- 728 Gao, S. (2009a). Geomorphology and sedimentology of tidal flats. In G. M. E. Perillo, E. Wolanski, D.  
729 Cahoon, M. Brinson (Eds.), *Coastal wetlands: An ecosystem integrated approach* (pp. 295–316).  
730 Amsterdam: Elsevier.

- 731 Gao, S. (2009b). Modeling the preservation potential of tidal flat sedimentary records, Jiangsu coast,  
732 eastern China. *Continental Shelf Research*, 29(16), 1927–1936.  
733 <https://doi.org/10.1016/j.csr.2008.12.010>
- 734 Geleynse, N., Storms, J. E. A., Walstra, D.-J. R., Jagers, H. R. A., Wang, Z. B., & Stive, M. J. F. (2011).  
735 Controls on river delta formation; insights from numerical modelling. *Earth and Planetary Science*  
736 *Letters*, 302(1), 217–226. doi:10.1016/j.epsl.2010.12.013
- 737 Gräwe, U., Burchard, H., Müller, M., & Schuttelaars, H. M. (2014). Seasonal variability in M<sub>2</sub> and M<sub>4</sub>  
738 tidal constituents and its implications for the coastal residual sediment transport. *Geophysical*  
739 *Research Letters*, 41(15), 5563–5570. <https://doi.org/10.1002/2014GL060517>
- 740 Guillou, N., Chapalain, G., & Thais, L. (2009). Three-dimensional modeling of tide-induced suspended  
741 transport of seabed multicomponent sediments in the eastern English Channel. *Journal of*  
742 *Geophysical Research*, 114, C07025. doi:10.1029/2008JC004791
- 743 Hayes, M. O. (1979). Barrier island morphology as a function of tidal and wave regime. In S. P.  
744 Leatherman (Ed.), *Barrier islands from the Gulf of St. Lawrence to the Gulf of Mexico* (pp. 211–  
745 236). New York: Academic Press.
- 746 Hsu, T.-J., Chen, S.-N., & Ogston, A. S. (2013). The landward and seaward mechanisms of fine-sediment  
747 transport across intertidal flats in the shallow-water region—A numerical investigation. *Continental*  
748 *Shelf Research*, 60, S85–S98. <https://doi.org/10.1016/j.csr.2012.02.003>
- 749 Hu, Z., Wang, Z. B., Zitman, T. J., Stive, M. J. F., & Bouma, T. J. (2015). Predicting long-term and short-  
750 term tidal flat morphodynamics using a dynamic equilibrium theory. *Journal of Geophysical*  
751 *Research: Earth Surface*, 120(9), 1803–1823. <https://doi.org/10.1002/2015JF003486>
- 752 Kim, B.-G., & Cho, Y.-K. (2017). Tide-induced residual circulation in a bay with laterally asymmetric  
753 depth. *Journal of Geophysical Research: Oceans*, 122(5), 4040–4050.  
754 <https://doi.org/10.1002/2016JC012473>
- 755 Kirby, R. (2000). Practical implications of tidal flat shape. *Continental Shelf Research*, 20(10), 1061-  
756 1077. [https://doi.org/10.1016/S0278-4343\(00\)00012-1](https://doi.org/10.1016/S0278-4343(00)00012-1)
- 757 Kirwan, M. L., & Murray, A. B. (2007). A coupled geomorphic and ecological model of tidal marsh  
758 evolution. *Proceedings of the National Academy of Sciences*, 104(15), 6118–6122.  
759 doi:10.1073/pnas.0700958104



- 760 Le Hir, P., Cayocca, F., & Waeles, B. (2011). Dynamics of sand and mud mixtures: A multiprocess-based  
761 modelling strategy. *Continental Shelf Research*, 31(10, Supplement), S135–S149.  
762 <https://doi.org/10.1016/j.csr.2010.12.009>
- 763 Le Hir, P., Monbet, Y., & Orvain, F. (2007). Sediment erodability in sediment transport modelling: Can  
764 we account for biota effects? *Continental Shelf Research*, 27(8), 1116–1142.  
765 <https://doi.org/10.1016/j.csr.2005.11.016>
- 766 Le Hir, P., Roberts, W., Cazaillet, O., Christie, M., Bassoullet, P., & Bacher, C. (2000). Characterization  
767 of intertidal flat hydrodynamics. *Continental Shelf Research*, 20(12), 1433–1459.  
768 [https://doi.org/10.1016/S0278-4343\(00\)00031-5](https://doi.org/10.1016/S0278-4343(00)00031-5)
- 769 Lesser, G. R., Roelvink, J. A., van Kester, J. A. T. M., & Stelling, G. S. (2004). Development and  
770 validation of a three-dimensional morphological model. *Coastal Engineering*, 51(8), 883–915.  
771 <https://doi.org/10.1016/j.coastaleng.2004.07.014>
- 772 Li, C., & O'Donnell, J. (2005). The effect of channel length on the residual circulation in tidally  
773 dominated channels. *Journal of Physical Oceanography*, 35(10), 1826–1840.  
774 <https://doi.org/10.1175/JPO2804.1>
- 775 Li, C., & O'Donnell, J. (1997). Tidally driven residual circulation in shallow estuaries with lateral depth  
776 variation. *Journal of Geophysical Research: Oceans*, 102(C13), 27915–27929.  
777 <https://doi.org/10.1029/97JC02330>
- 778 Liu, Z. Huang, Y., & Zhang, Q. (1989). Tidal current ridges in the southwestern Yellow Sea. *Journal of*  
779 *Sedimentary Research*, 59(3), 432–437. [https://doi.org/10.1306/212F8FB7-2B24-11D7-](https://doi.org/10.1306/212F8FB7-2B24-11D7-8648000102C1865D)  
780 [8648000102C1865D](https://doi.org/10.1306/212F8FB7-2B24-11D7-8648000102C1865D)
- 781 Maan, D. C., van Prooijen, B. C., Wang, Z. B., & De Vriend, H. J. (2015). Do intertidal flats ever reach  
782 equilibrium? *Journal of Geophysical Research: Earth Surface*, 120(11), 2406–2436.  
783 <https://doi.org/10.1002/2014JF003311>
- 784 Mangor, K., Drønen, N. K., Kærgaard, K. H., & Kristensen, S. E. (2017). *Shoreline management*  
785 *guidelines*. Hørsholm: DHI.
- 786 Marani, M., D'Alpaos, A., Lanzoni, S., Carniello, L., & Rinaldo, A. (2010). The importance of being  
787 coupled: Stable states and catastrophic shifts in tidal biomorphodynamics. *Journal of Geophysical*  
788 *Research: Earth Surface*, 115(F4). <https://doi.org/10.1029/2009JF001600>
- 789 Marion, C., Anthony, E. J., & Trentesaux, A. (2009). Short-term ( $\leq 2$  yrs) estuarine mudflat and saltmarsh  
790 sedimentation: High-resolution data from ultrasonic altimetry, rod surface-elevation table, and filter

- 791 traps. *Estuarine, Coastal and Shelf Science*, 83(4), 475–484.  
792 <https://doi.org/10.1016/j.ecss.2009.03.039>
- 793 Mariotti, G., & Fagherazzi, S. (2010). A numerical model for the coupled long-term evolution of salt  
794 marshes and tidal flats. *Journal of Geophysical Research: Earth Surface*, 115(F1).  
795 <https://doi.org/10.1029/2009JF001326>
- 796 Mudd, S. M., D'Alpaos, A., & Morris, J. T. (2010). How does vegetation affect sedimentation on tidal  
797 marshes? Investigating particle capture and hydrodynamic controls on biologically mediated  
798 sedimentation. *Journal of Geophysical Research: Earth Surface*, 115(F3).  
799 <https://doi.org/10.1029/2009JF001566>
- 800 Nittrouer, C. A., Raubenheimer, B., & Wheatcroft, R. A. (2013). Lessons learned from comparisons of  
801 mesotidal sand- and mudflats. *Continental Shelf Research*, 60, S1-S12.  
802 <https://doi.org/10.1016/j.csr.2013.03.003>
- 803 Olabarrieta, M., Geyer, W. R., Coco, G., Friedrichs, C. T., & Cao, Z. (2018). Effects of density - driven  
804 flows on the long - term morphodynamic evolution of funnel - shaped estuaries. *Journal of*  
805 *Geophysical Research: Earth Surface*, 123, 2901–2924. <https://doi.org/10.1029/2017JF004527>
- 806 Paarlberg, A. J., Knaapen, M. A. F., de Vries, M. B., Hulscher, S. J. M. H., & Wang, Z. B. (2005).  
807 Biological influences on morphology and bed composition of an intertidal flat. *Estuarine, Coastal*  
808 *and Shelf Science*, 64(4), 577–590. <https://doi.org/10.1016/j.ecss.2005.04.008>
- 809 Partheniades, E. (1965). Erosion and deposition of cohesive soils. *Journal of the Hydraulics Division*,  
810 91(1), 105–139.
- 811 Pritchard, D., & Hogg, A. J. (2003). Cross-shore sediment transport and the equilibrium morphology of  
812 mudflats under tidal currents. *Journal of Geophysical Research: Oceans*, 108(C10).  
813 <https://doi.org/10.1029/2002JC001570>
- 814 Pritchard, D., Hogg, A. J., & Roberts, W. (2002). Morphological modelling of intertidal mudflats: the role  
815 of cross-shore tidal currents. *Continental Shelf Research*, 22(11), 1887–1895.  
816 [https://doi.org/10.1016/S0278-4343\(02\)00044-4](https://doi.org/10.1016/S0278-4343(02)00044-4)
- 817 Quaresma, V. d. S., Bastos, A. C., & Amos, C. L. (2007). Sedimentary processes over an intertidal flat: A  
818 field investigation at Hythe flats, Southampton Water (UK). *Marine Geology*, 241(1), 117–136.  
819 <https://doi.org/10.1016/j.margeo.2007.03.009>
- 820 Reise, K. (2001). *Ecological comparison of sedimentary shores*. Berlin: Springer-Verlag.

- 821 Ren, M. E. (Ed.) (1986). *Comprehensive investigation of the coastal zone and tidal land resources of*  
822 *Jiangsu Province* (in Chinese). Beijing: Ocean Press.
- 823 Ren, M. E., Zhang, R. S., & Yang, J. H. (1985). Effect of typhoon no. 8114 on coastal morphology and  
824 sedimentation of Jiangsu Province, People's Republic of China. *Journal of Coast Research*, 1(1),  
825 21–28.
- 826 Roberts, W., Le Hir, P., & Whitehouse, R. J. S. (2000). Investigation using simple mathematical models  
827 of the effect of tidal currents and waves on the profile shape of intertidal mudflats. *Continental Shelf*  
828 *Research*, 20(10), 1079–1097. [https://doi.org/10.1016/S0278-4343\(00\)00013-3](https://doi.org/10.1016/S0278-4343(00)00013-3)
- 829 Robinson, A. H. W. (1960). Ebb-flood channel systems in sandy bays and estuaries. *Geography*, 45(3),  
830 183–199.
- 831 Roelvink, J. A. (2006). Coastal morphodynamic evolution techniques. *Coastal Engineering*, 53(2), 277–  
832 287. <https://doi.org/10.1016/j.coastaleng.2005.10.015>
- 833 Rossi, V. M., Kim, W., López, J. L., Edmonds, D., Geleynse, N., Olariu, C., et al. (2016). Impact of tidal  
834 currents on delta-channel deepening, stratigraphic architecture, and sediment bypass beyond the  
835 shoreline. *Geology*, 44, 927–930. doi: 10.1130/G38334.1
- 836 Schwarz, C., Ye, Q. H., van der Wal, D., Zhang, L. Q., Bouma, T., Ysebaert, T., & Herman, P. M. J.  
837 (2014). Impacts of salt marsh plants on tidal channel initiation and inheritance. *Journal of*  
838 *Geophysical Research: Earth Surface*, 119(2), 385–400. <https://doi.org/10.1002/2013JF002900>
- 839 Shi, B. W., Yang, S. L., Wang, Y. P., Li, G. C., Li, M. L., Li, P., & Li, C. (2017). Role of wind in  
840 erosion-accretion cycles on an estuarine mudflat. *Journal of Geophysical Research: Oceans*, 122(1),  
841 193–206. <https://doi.org/10.1002/2016JC011902>
- 842 Tambroni, N., & Seminara, G. (2012). A one-dimensional eco-geomorphic model of marsh response to  
843 sea level rise: Wind effects, dynamics of the marsh border and equilibrium. *Journal of Geophysical*  
844 *Research: Earth Surface*, 117(F3). <https://doi.org/10.1029/2012JF002363>
- 845 Tejedor, A., Longjas, A., Caldwell, R., Edmonds, D. A., Zaliapin, I., & Foufoula-Georgiou, E. (2016).  
846 Quantifying the signature of sediment composition on the topologic and dynamic complexity of river  
847 delta channel networks and inferences toward delta classification. *Geophysical Research Letters*, 43,  
848 3280–3287. doi:10.1002/2016GL068210
- 849 Temmerman, S., Meire, P., Bouma, T. J., Herman, P. M. J., Ysebaert, T., & De Vriend, H. J. (2013).  
850 Ecosystem-based coastal defence in the face of global change. *Nature*, 504, 79–83.  
851 <https://doi.org/10.1038/nature12859>

- 852 Ulses, C., Estournel, C., Durrieu de Madron, X., & Palanques, A. (2008). Suspended sediment transport  
853 in the Gulf of Lions (NW Mediterranean): Impact of extreme storms and floods. *Continental Shelf*  
854 *Research*, 28(15), 2048–2070. <https://doi.org/10.1016/j.csr.2008.01.015>
- 855 van der Wegen, M., & Jaffe, B. E. (2014). Processes governing decadal-scale depositional narrowing of  
856 the major tidal channel in San Pablo Bay, California, USA. *Journal of Geophysical Research: Earth*  
857 *Surface*, 119(5), 1136–1154. <https://doi.org/10.1002/2013JF002824>
- 858 van Kessel, T., Spruyt-de Boer, A., van der Werf, J., Sittoni, L., van Prooijen, B. C., Winterwerp, H.  
859 (2012). *Bed module for sand-mud mixtures, in framework of BwN project NTW 1.3 mud dynamics*  
860 (draft). Delft: Deltares.
- 861 van Ledden, M., van Kesteren, W. G. M., & Winterwerp, J. C. (2004). A conceptual framework for the  
862 erosion behaviour of sand–mud mixtures. *Continental Shelf Research*, 24(1), 1–11.  
863 <https://doi.org/10.1016/j.csr.2003.09.002>
- 864 van Ledden, M., Wang, Z.-B., Winterwerp, H., & de Vriend, H. (2006). Modelling sand–mud  
865 morphodynamics in the Friesche Zeegat. *Ocean Dynamics*, 56(3), 248–265.  
866 <https://doi.org/10.1007/s10236-005-0055-9>
- 867 van Rijn, L. C. (2007). Unified View of Sediment Transport by Currents and Waves. I: Initiation of  
868 Motion, Bed Roughness, and Bed-Load Transport. *Journal of Hydraulic Engineering*, 133(6), 649–  
869 667. [https://doi.org/10.1061/\(ASCE\)0733-9429\(2007\)133:6\(649\)](https://doi.org/10.1061/(ASCE)0733-9429(2007)133:6(649))
- 870 Wang, A., Gao, S., Chen, J., & Li, D. (2009). Sediment dynamic responses of coastal salt marsh to  
871 typhoon “KAEMI” in Quanzhou Bay, Fujian Province, China. *Chinese Science Bulletin*, 54(1), 120–  
872 130. <https://doi.org/10.1007/s11434-008-0365-7>
- 873 Wang, X. H., Qiao, F., Lu, J., & Gong, F. (2011). The turbidity maxima of the northern Jiangsu shoal-  
874 water in the Yellow Sea, China. *Estuarine, Coastal and Shelf Science*, 93(3), 202–211.  
875 <https://doi.org/10.1016/j.ecss.2010.10.020>
- 876 Wang, X., & Ke, X. (1997). Grain-size characteristics of the extant tidal flat sediments along the Jiangsu  
877 coast, China. *Sedimentary Geology*, 112(1), 105–122. [https://doi.org/10.1016/S0037-](https://doi.org/10.1016/S0037-0738(97)00026-2)  
878 [0738\(97\)00026-2](https://doi.org/10.1016/S0037-0738(97)00026-2)
- 879 Wang, Y. P., Gao, S., Jia, J., Thompson, C. E. L., Gao, J., & Yang, Y. (2012). Sediment transport over an  
880 accretional intertidal flat with influences of reclamation, Jiangsu coast, China. *Marine Geology*, 291–  
881 294, 147–161. <https://doi.org/10.1016/j.margeo.2011.01.004>

- 882 Wang, Y., Gao, S., & Jia, J. (2006). High-resolution data collection for analysis of sediment dynamic  
883 processes associated with combined current-wave action over intertidal flats. *Chinese Science*  
884 *Bulletin*, 51(7), 866–877. <https://doi.org/10.1007/s11434-006-0866-1>
- 885 Wang, Y., Yu, Q., Gao, S., & Flemming, B. (2014). Modeling the effect of progressive grain-size sorting  
886 on the scale dependence of back-barrier tidal basin morphology. *Continental Shelf Research*, 91, 26–  
887 36. <https://doi.org/10.1016/j.csr.2014.09.006>
- 888 Wang, Y., Yu, Q., Jiao, J., Tonnon, P. K., Wang, Z. B., & Gao, S. (2016). Coupling bedform roughness  
889 and sediment grain-size sorting in modelling of tidal inlet incision. *Marine Geology*, 381, 128–141.  
890 <https://doi.org/10.1016/j.margeo.2016.09.004>
- 891 Wang, Y., Zhang, Y., Zou, X., Zhu, D., & Piper, D. (2012). The sand ridge field of the South Yellow Sea:  
892 Origin by river–sea interaction. *Marine Geology*, 291–294, 132–146.  
893 <https://doi.org/10.1016/j.margeo.2011.01.001>
- 894 Wang, Z. B. (1992). Theoretical analysis on depth-integrated modelling of suspended sediment transport.  
895 *Journal of Hydraulic Research*, 30(3), 403–421. <https://doi.org/10.1080/00221689209498927>
- 896 Xing, F., Wang, Y. P., & Wang, H. V. (2012). Tidal hydrodynamics and fine-grained sediment transport  
897 on the radial sand ridge system in the southern Yellow Sea. *Marine Geology*, 291–294, 192–210.  
898 <https://doi.org/10.1016/j.margeo.2011.06.006>
- 899 Xing, F., Wang, Y., Gao, J., & Zou, X. (2010). Seasonal distributions of the concentrations of suspended  
900 sediment along Jiangsu coastal sea (in Chinese with English abstract). *Oceanologia et Limnologia*  
901 *Sinica*, 41(3), 1–10.
- 902 Yang, S. L., Li, H., Ysebaert, T., Bouma, T. J., Zhang, W. X., Wang, Y. Y., et al. (2008). Spatial and  
903 temporal variations in sediment grain size in tidal wetlands, Yangtze Delta: On the role of physical  
904 and biotic controls. *Estuarine, Coastal and Shelf Science*, 77(4), 657–671.  
905 <https://doi.org/10.1016/j.ecss.2007.10.024>
- 906 Yang, S.-L., Friedrichs, C. T., Shi, Z., Ding, P.-X., Zhu, J., & Zhao, Q.-Y. (2003). Morphological  
907 response of tidal marshes, flats and channels of the Outer Yangtze River mouth to a major storm.  
908 *Estuaries*, 26(6), 1416–1425. <https://doi.org/10.1007/BF02803650>
- 909 Yu, Q., Flemming, B. W., & Gao, S. (2011). Tide-induced vertical suspended sediment concentration  
910 profiles: phase lag and amplitude attenuation. *Ocean Dynamics*, 61(4), 403–410.  
911 <https://doi.org/10.1007/s10236-010-0335-x>

- 912 Yu, Q., Wang, Y. P., Flemming, B., & Gao, S. (2012). Tide-induced suspended sediment transport:  
913 Depth-averaged concentrations and horizontal residual fluxes. *Continental Shelf Research*, 34, 53–  
914 63. <https://doi.org/10.1016/j.csr.2011.11.015>
- 915 Yu, Q., Wang, Y. W., & Gao, S. (2014). Tide and continental shelf circulation induced suspended  
916 sediment transport on the Jiangsu Coast: winter observations out of Xinyanggang (in Chinese, with  
917 English abstract). *Journal of Nanjing University (natural sciences)*, 50, 625–634.
- 918 Yu, Q., Wang, Y., Shi, B., Wang, Y. P., & Gao, S. (2017). Physical and sedimentary processes on the  
919 tidal flat of central Jiangsu Coast, China: Headland induced tidal eddies and benthic fluid mud  
920 layers. *Continental Shelf Research*, 133, 26–36. <https://doi.org/10.1016/j.csr.2016.12.015>
- 921 Zhang, R. (1992). Suspended sediment transport processes on tidal mud flat in Jiangsu Province, China.  
922 *Estuarine, Coastal and Shelf Science*, 35(3), 225–233. [https://doi.org/10.1016/S0272-](https://doi.org/10.1016/S0272-7714(05)80045-9)  
923 [7714\(05\)80045-9](https://doi.org/10.1016/S0272-7714(05)80045-9)
- 924 Zimmerman, J. T. F. (1974). Circulation and water exchange near a tidal watershed in the dutch wadden  
925 sea. *Netherlands Journal of Sea Research*, 8(2), 126–138. [https://doi.org/10.1016/0077-](https://doi.org/10.1016/0077-7579(74)90013-1)  
926 [7579\(74\)90013-1](https://doi.org/10.1016/0077-7579(74)90013-1)
- 927

928 **Figure captions**

929 **Figure 1.** Sketch of sand-mud tidal flat influenced by cross-shore and alongshore tidal currents  
 930 (MHWL, MWL, and MLWL denotes mean high water level, mean water level and mean low  
 931 water level, respectively, modified from Friedrichs (2011)).

932 **Figure 2.** (a) Maps of the study area and the location of the intertidal flats at Dafeng, Jiangsu,  
 933 China; (b) Sites of field measurements in 2008: A08, M08, and S1/S3 are anchor stations for  
 934 hydrodynamic measurements, and P1 is the bed level profile (modified from Wang Y.P. et al.  
 935 (2012)).

936 **Figure 3.** Grid and initial bathymetry (O1, O2, and O3: observation points, CS: cross-section,  
 937 red rectangle: focused area. Bed elevation: 0 m refers to the mean sea level).

938 **Figure 4.** Observed and modeled bed elevation and sand content of surface sediment along the  
 939 profile P1 in Figure 2b (The observed elevation is with reference to the national datum1985, in  
 940 which 0 m is the long-term mean sea level of the Yellow Sea).

941 **Figure 5.** Observational hydrodynamics: time series of water depth, depth-averaged velocity,  
 942 and SSC measured at the upper (A08, blue line), middle (M08, green line), and lower (S1/S3, red  
 943 line) intertidal flat. Locations of the stations are marked in Figure 2b.  $V_c$  and  $V_l$  are the current  
 944 velocity components across (offshore (ebb) “+” and onshore (flood) “-”) and along (northward  
 945 (ebb) “+” and southward (flood) “-”) the intertidal flat, respectively.

946 **Figure 6.** (a, b, c, d) Modeled bathymetry in the focused area in Figure 3; (e, f, g, h) Bed  
 947 elevation and stratigraphy of the cross-section CS.

948 **Figure 7.** Temporal variations of (a) bed elevation and (b) sand content of surface sediment  
 949 along the cross-shore profile CS.

950 **Figure 8.** Modeled hydrodynamics: time series of water depth, depth-averaged velocity, and SSC  
 951 at O1 (blue line), O2 (green line), and O3 (red line) during a tidal cycle from the 1<sup>st</sup> year in the  
 952 flat’s evolution of the reference case.  $V_c$  and  $V_l$  are the current velocity components across  
 953 (offshore (ebb) “+” and onshore (flood) “-”) and along (northward (ebb) “+” and southward  
 954 (flood) “-”) the intertidal flat, respectively. Areas in light yellow are estimated ADCP blanking  
 955 at S1/S3 (Figure 2b and 5), corresponding to water depth smaller than 1.5 m.

956 **Figure 9.** Comparison of (a) bed elevation, (b) sand content of surface sediment; tidally  
957 maximum flood current speed (c) alongshore and (d) cross-shore; and (e) tidally maximum bed  
958 shear stress magnitude along the cross-shore profile CS at the 4th year in the three cases. The  
959 dashed arrows indicate the turning points of  $\tau_{\max}$  in the  $12^\circ$  and  $16^\circ$  cases, which are also  
960 corresponding to the transitions between mud and sand flat.

961 **Figure 10.** Modeled hydrodynamics (based on the 1st year bathymetry and hydrodynamic  
962 conditions of the reference case) along the cross-shore profile CS: tidally maximum flood current  
963 speed (a) alongshore and (b) cross-shore; tidally averaged SSC of (c) mud and (d) sand; and  
964 variations of available mass of (e) mud and (f) sand in a tidal cycle.



Figure 1.

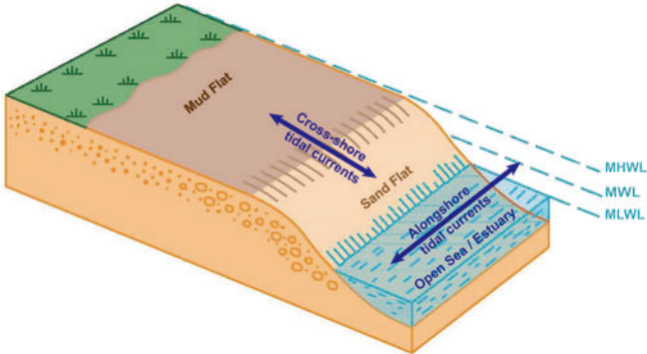


Figure 2.

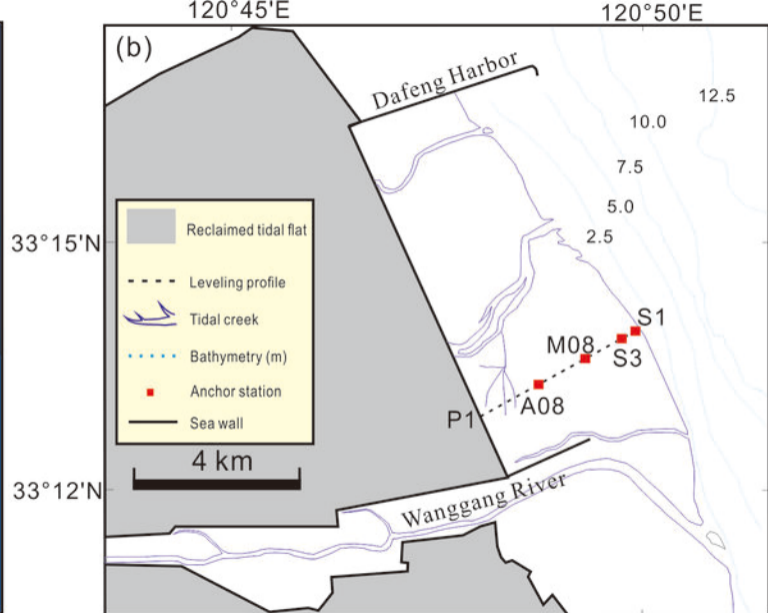
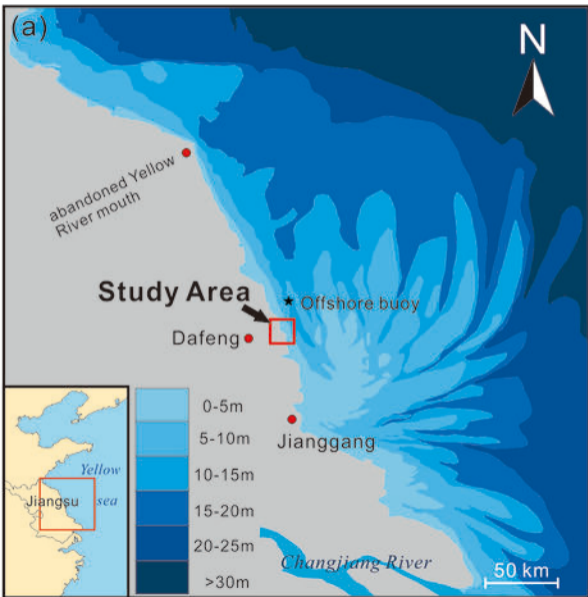


Figure 3.



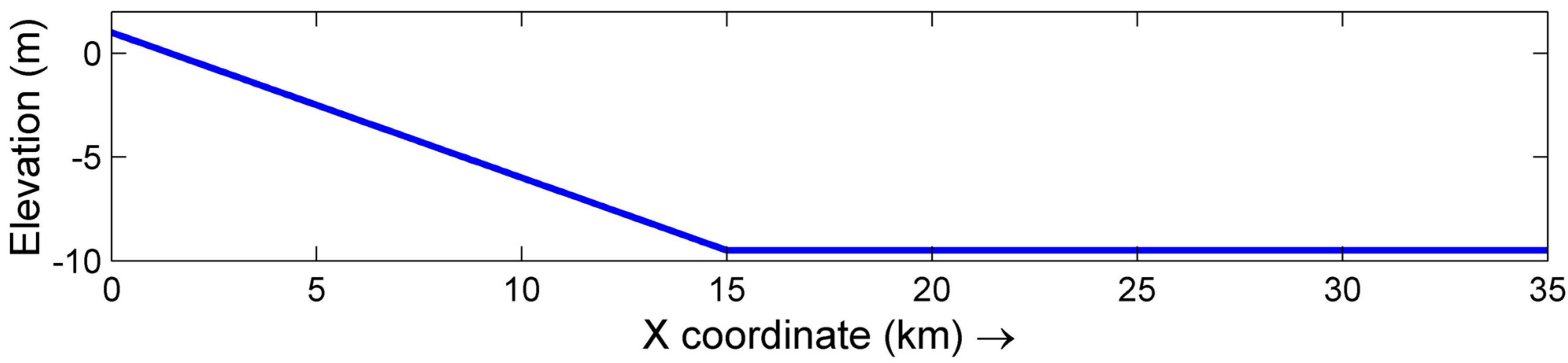
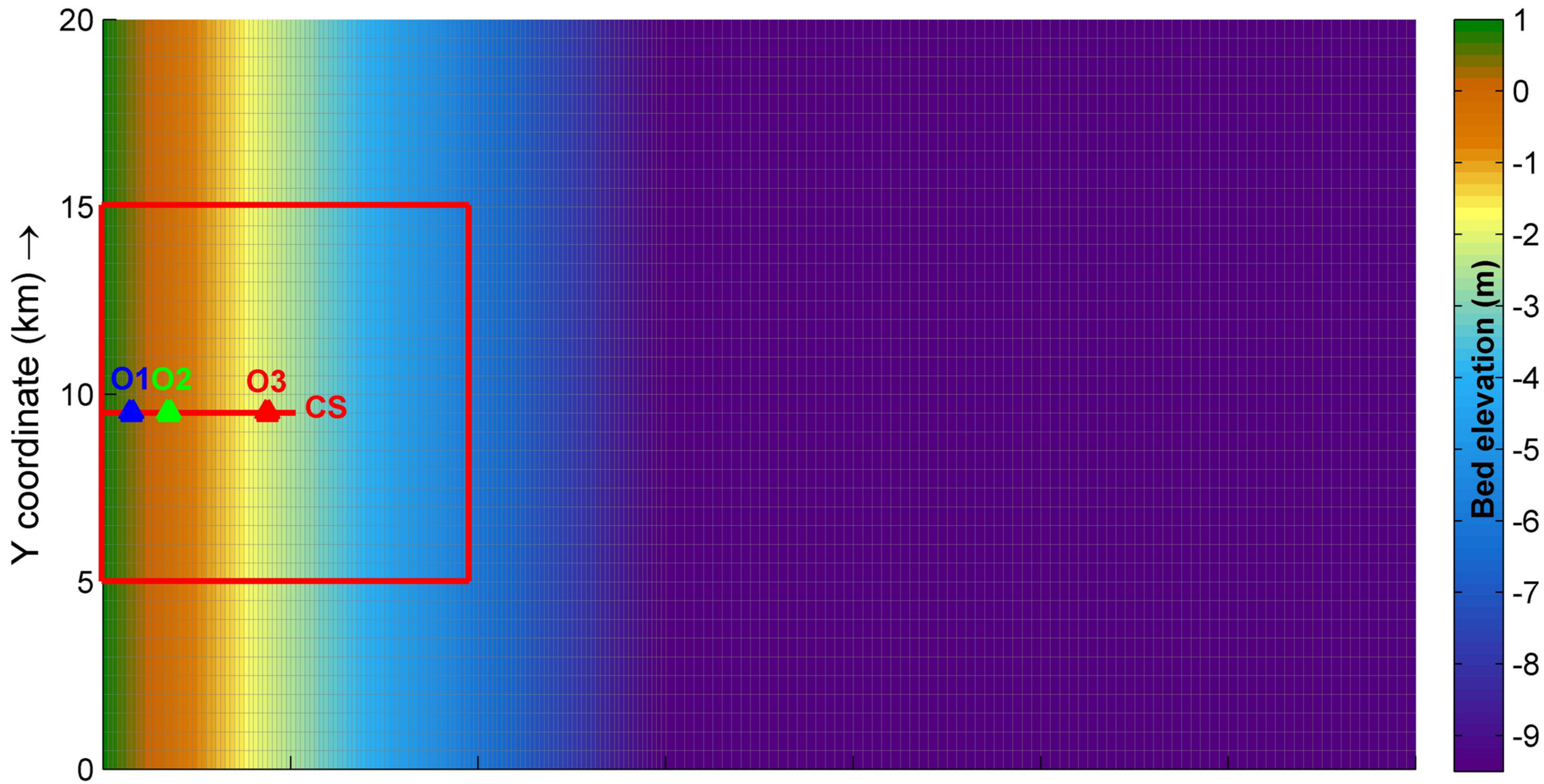
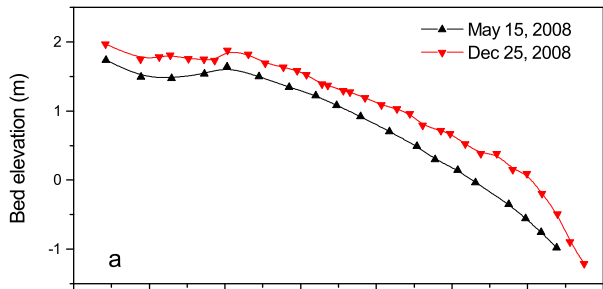




Figure 4.

### Observed



### Modeled

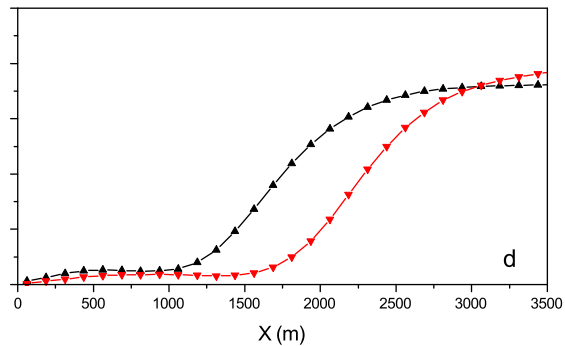
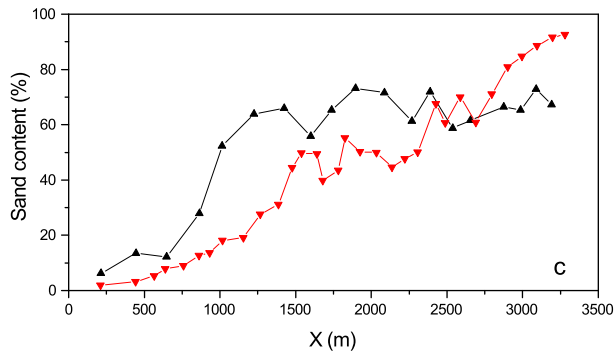
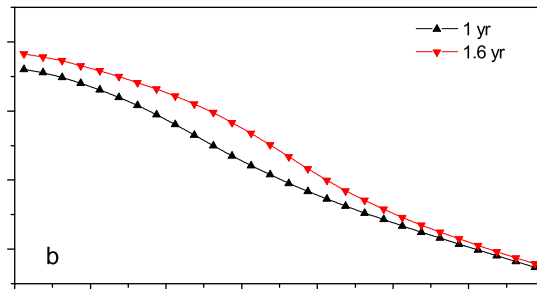




Figure 5.

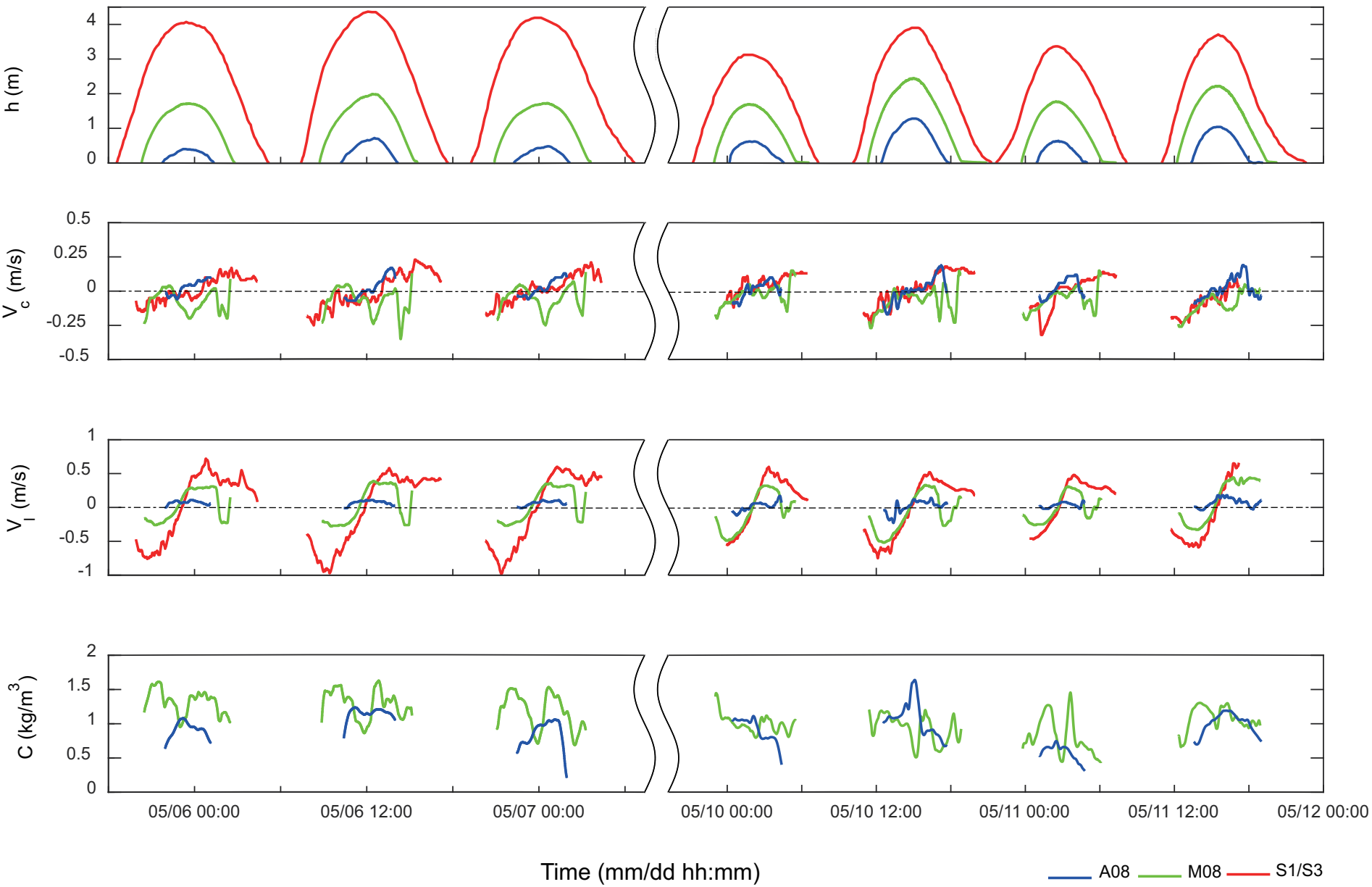
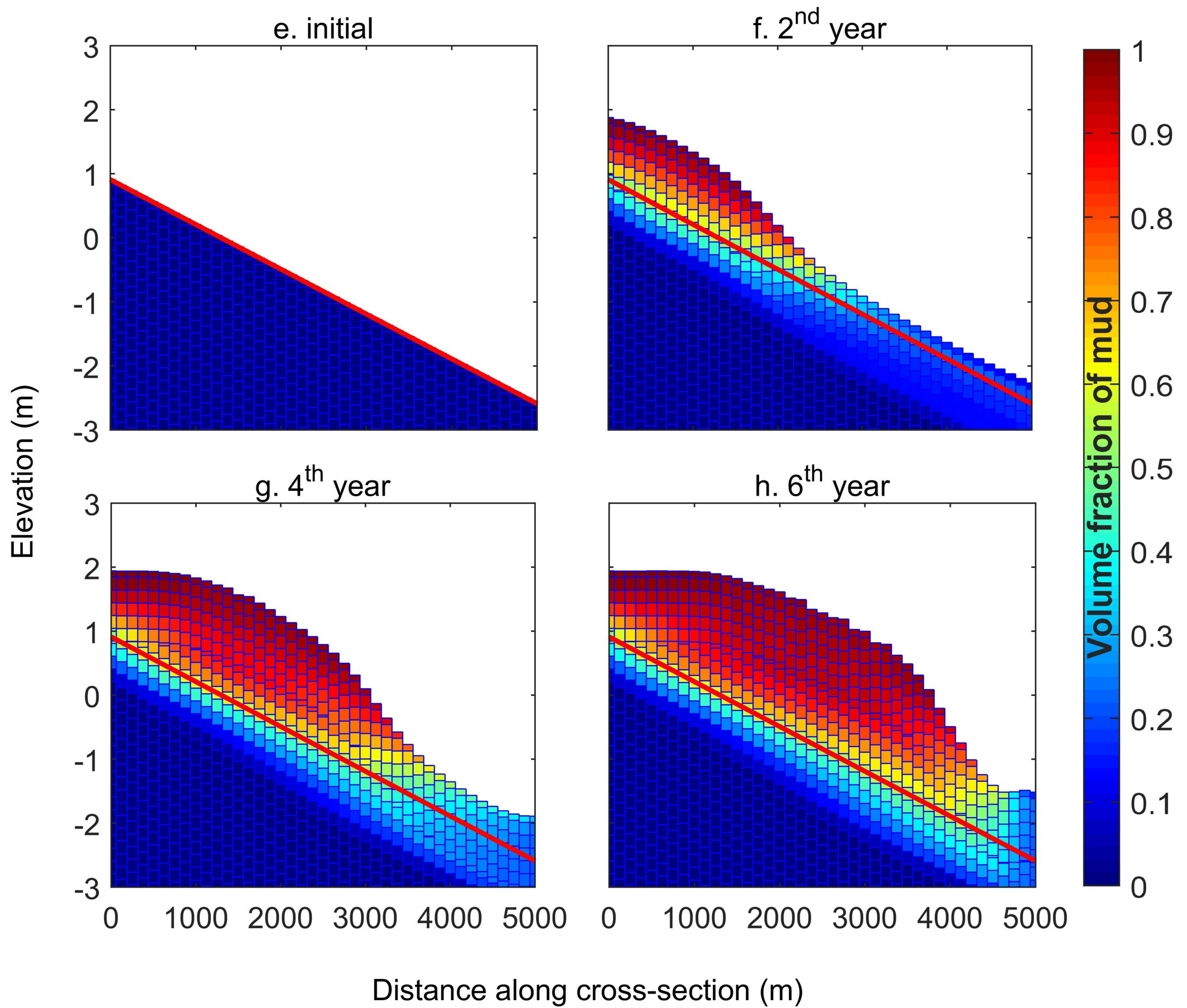
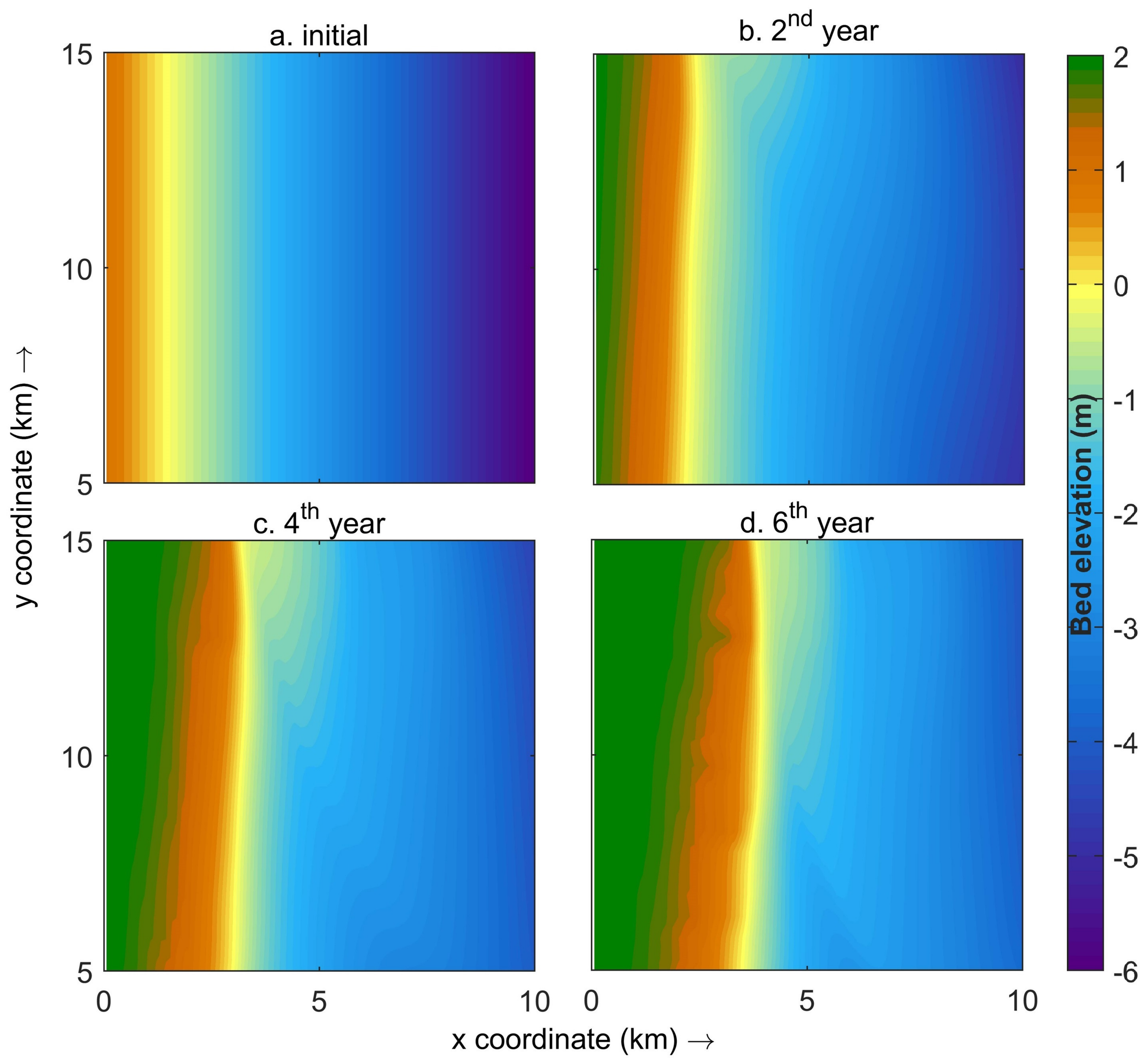


Figure 6.







**Figure 7.**

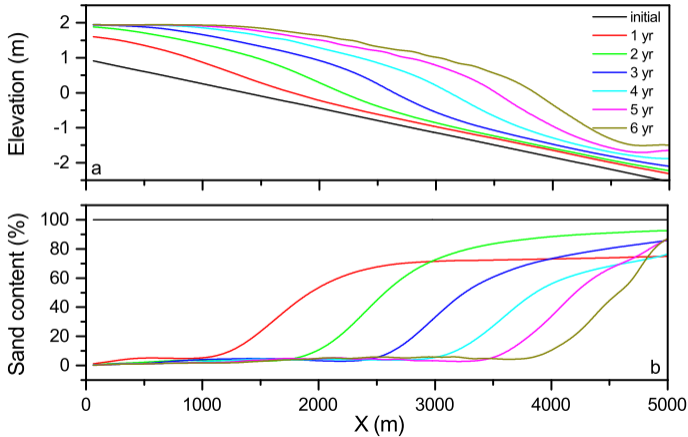


Figure 8.

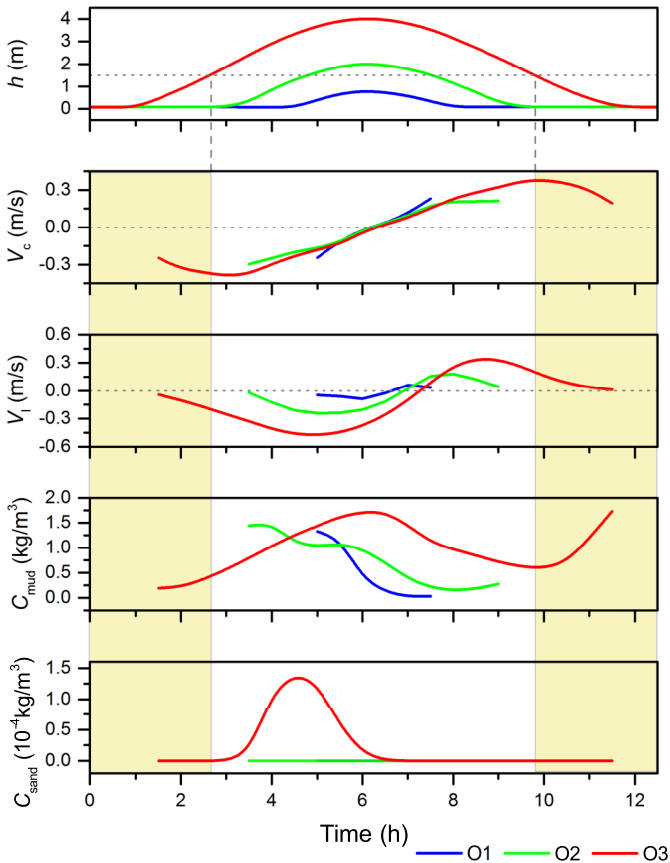




Figure 9.

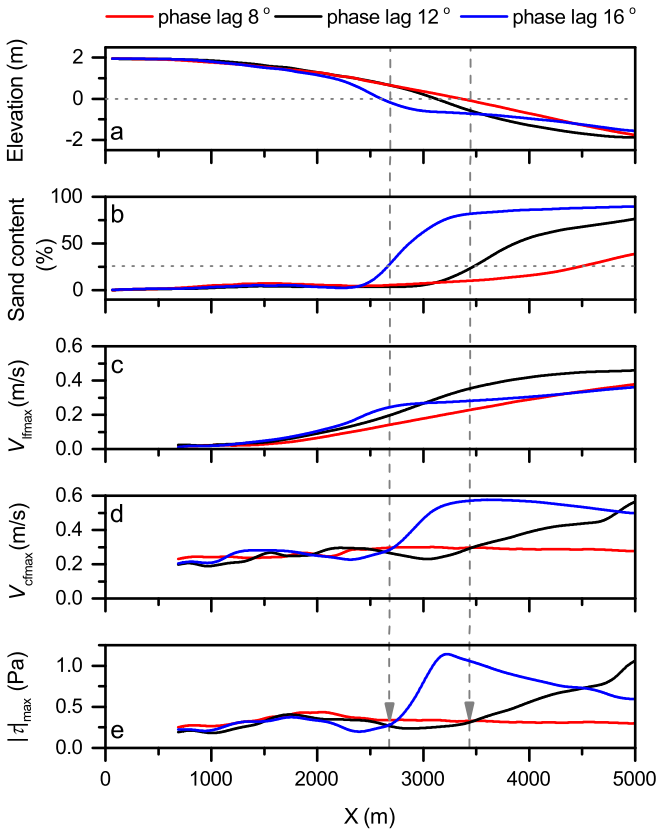


Figure 10.

